Improving low-quality satellite remote sensing reflectance at blue bands over coastal and inland waters

Jianwei Wei [1,2*], Xiaolong Yu [3], Zhongping Lee [4], Menghua Wang [1], and Lide Jiang [1,5]

[1] *NOAA Center for Satellite Applications and Research, College Park, MD 20740, USA*

[2] *Global Science & Technology Inc., Greenbelt, MD 20770, USA*

[3] *Xiamen University, State Key Laboratory of Marine Environmental Science, Xiamen, 361102, China*

[4] *School for the Environment, University of Massachusetts Boston, Boston, MA 02125, USA*

[5] *Colorado State University, Cooperative Institute for Research in the Atmosphere, Fort Collins, CO 80523, USA*

* *Correspondence: jianwei.wei@noaa.gov*

Abstract

The satellite remote sensing reflectance ($R_{rs}(\lambda)$) at two short blue bands (410 or 412 nm and 443 nm) are prone to large uncertainties in coastal and inland waters, prohibiting algorithms from generating reliable ocean color products associated with these bands. In this study, we developed an algorithm to estimate R_{rs}(41x) and R_{rs}(443) when the satellite $R_{rs}(\lambda)$ in blue bands suffer from large uncertainties. The algorithm first determines the $R_{rs}(\lambda)$ spectral shape from the satellite-measured $R_{rs}(\lambda)$ values at three wavelengths of 48x (486, 488, or 490), 55x (547, 551, or 555), and 67x (667, 670, or 671) nm. The algorithm then derives R_{rs}(41x) and R_{rs}(443) from the estimated $R_{rs}(\lambda)$ spectral shape with algebraic formulations. We assessed the algorithm performance with satellite (SeaWiFS, MODISA, and VIIRS-SNPP) and *in situ* $R_{rs}(\lambda)$ matchups from global waters. It is shown that the uncertainties of estimated R_{rs}(41x) and R_{rs}(443) are substantially smaller than the original satellite products when applicable. Besides, implementation of the algorithm contributes to a significant increase in the number of utilizable R_{rs}(41x) and R_{rs}(443) values. The algorithm is relatively stable and is best applicable to the satellite $R_{rs}(\lambda)$ spectra for which the R_{rs}(48x) and R_{rs}(55x) measurements are subject to small uncertainties. The demonstrations support the application of the blue-band estimation algorithm to a wide range of coastal waters.

Keyword: Remote sensing reflectance; Blue bands; Spectral shape; Atmospheric correction; SeaWiFS; MODIS; VIIRS.

1. Introduction

Ocean color satellites provide a means of collecting remote sensing reflectance ($R_{rs}(\lambda)$) on spatial and temporal scales unattainable by conventional *in situ* measurements. The $R_{rs}(\lambda)$ data allow for the derivation of important biological and biogeochemical properties of the upper oceans, such as phytoplankton chlorophyll-a concentration (Chl) (Hu et al., 2012; McClain, 2009; Wang and Son, 2016), phytoplankton light absorption (Wang et al., 2017; Wei and Lee, 2015), colored dissolved organic matter (CDOM) absorption (Mannino et al., 2014; Wei et al., 2016a; Yu et al., 2016), and primary production (Behrenfeld et al., 2005; Lee et al., 2015a), etc. For reliable estimation of these bio-optical properties, it is vital to obtain accurate $R_{rs}(\lambda)$ product from satellites over a wide spectral domain, particularly at the blue bands of 41x (410 or 412) nm and 443 nm.

The ocean color satellites, including the decommissioned Sea-viewing Wide Field-of-view Sensor (SeaWiFS, 1997–2010) and the operational Moderate Resolution Imaging Spectroradiometer (MODIS) onboard the Aqua satellite (MODISA, 2002–present) and Visible Infrared Imaging Radiometer Suite (VIIRS) onboard the Suomi National Polar-orbiting Partnership satellite (VIIRS-SNPP, 2011–present), retrieve $R_{rs}(\lambda)$ from the radiance measured at the top of atmosphere (TOA) through atmospheric correction (AC). Operational AC algorithms usually start with the selection of an aerosol model by assuming null contribution of water-leaving radiance ($L_w(\lambda)$) at the near-infrared (NIR) or shortwave infrared (SWIR) bands (Antoine and Morel, 1999; Gordon and Wang, 1994; Wang, 2007; Wang and Shi, 2007). This "black-pixel" assumption works well in open oceans, but is faced with some difficulties in coastal regions using the NIR and SWIR approach. The strongly absorbing aerosols, for instance, can be prominent in the coastal waters near anthropogenic sources of fossil-burning products, soot, and smog, or under the influence of dust transport. The weakly or strongly absorbing aerosols are hardly discriminable from radiance measurements in the NIR/SWIR domain but quite distinctive at short blue wavelengths (IOCCG, 2010). That being said, the standard AC schemes cannot correctly estimate the strongly absorbing aerosols and often fail to yield robust $R_{rs}(\lambda)$ products at the blue wavelengths in many coastal regions due to lack of aerosol vertical distribution information (IOCCG, 2010; Kahn et al., 2016). As a consequence, and expectedly, the satellite-derived R_{rs}(41x) and R_{rs}(443) products are prone to large uncertainties in the coastal waters (Antoine et al., 2008; Feng et al., 2008; Hlaing et al., 2013; Qin et al., 2017; Zibordi et al., 2009). Apart from atmospheric correction, the large uncertainty in satellite R_{rs}(41x) product is also related to system vicarious calibration and instrument degradation (Franz et al., 2018). The relatively large uncertainties at blue bands and the subsequent lack of utilizable data at these two bands add to the difficulties of satellite ocean color applications in coastal regions (Mouw et al., 2015).

To address the blue-band $R_{rs}(\lambda)$ quality issues, a great deal of effort has been invested. Gordon et al. (1997) and Chomko and Gordon (2001) developed an AC procedure to quantify the strongly absorbing aerosol contribution under dust-dominating conditions. Application of their methods, however, remains impractical because the vertical distribution of absorbing aerosols in the atmosphere is not known *a priori* (Banzon et al., 2009; IOCCG, 2010). In another case study, Hu et al. (2000) tested a nearest-neighbor method to account for the aerosol contribution at the NIR bands, with reasonable results. Variants of the standard AC schemes also emerged. Oo et al. (2008) reported improved atmospheric correction for turbid coastal waters by placing constraints onto R_{rs}(412) within their AC procedures. For highly absorptive waters, He et al. (2012) proposed null water-leaving radiance at 412 nm so as to make a guess of the aerosol contribution at that band, which was then used for atmospheric correction. In analogy, Wang and Jiang (2018) forced the negative $R_{rs}(410)$ values from VIIRS-SNPP to zeroes to estimate the aerosol contributions and ultimately to obtain improved $R_{rs}(\lambda)$ products.

Besides the above contributions, there exists another line of methodology to deal with the blue-band $R_{rs}(\lambda)$ measurements. Basically, this category of methods attempts to "correct" the problematic blue-band $R_{rs}(\lambda)$ data. In this regard, Ransibrahmanakul and Stumpf (2006) tested a power-law function to account for the spectral artifacts caused by the absorbing aerosols in the northeast U.S. coasts. D'Alimonte et al. (2008) derived multi-linear regression coefficients from satellite and *in situ* $R_{rs}(\lambda)$ matchups and further applied those coefficients to estimate $R_{rs}(412)$ for the same region. Undoubtedly, all strategies mentioned above have demonstrated varying degrees of success, specific to the sensors, dataset, or environments, in improving blue-band $R_{rs}(\lambda)$ quality. Yet, it remains an open question to implement such algorithms as a universal approach to global coastal and inland waters where the satellite $R_{rs}(41\text{x})$ and $R_{rs}(443)$ data are of low quality.

The blue-band $R_{rs}(\lambda)$ data are needed for many bio-optical retrievals in the upper water columns. Among others, $R_{rs}(41\text{x})$ and $R_{rs}(443)$ are indispensable for many semi-analytical algorithms to retrieve the phytoplankton and CDOM absorption coefficients from multiband satellite $R_{rs}(\lambda)$ (IOCCG, 2006; Lee et al., 2002; Wei et al., 2019; Werdell et al., 2013). $R_{rs}(443)$ data may also be required for Chl estimation in both open and coastal oceans (Hu et al., 2012; O'Reilly et al., 1998; Wang and Son, 2016). Use of $R_{rs}(41\text{x})$ and $R_{rs}(443)$ data with large errors can result in unrealistic retrievals for the water bio-optical properties (Werdell et al., 2018) and biased Chl products (Hyde et al., 2007). It is also risky that merging of such satellite products may generate spurious trends in ocean color time series. In order to best interpret the large-scale and long-term ocean color retrievals, this long-standing problem associated with the blue-band satellite $R_{rs}(\lambda)$ measurements needs to be resolved.

In this study, we propose a spectral shape based algorithm to estimate R_{rs}(41x) and R_{rs}(443) when the satellite $R_{rs}(\lambda)$ spectra at blue bands are subjected to large uncertainties. Such estimation will help ultimately enhance the bio-optical retrievals with the ocean color algorithms requiring R_{rs}(41x) and/or R_{rs}(443) data. In the following, we first describe the evaluation data from SeaWiFS, MODISA, and VIIRS-SNPP, the proposed algorithm, and relevant analyses (Section 2). Next, we demonstrate the algorithm performance in estimating R_{rs}(41x) and R_{rs}(443) by comparison with *in situ* matchup measurements (Section 3). Finally, we discuss the algorithm applicability, uncertainty, potential impacts on satellite bio-optical retrievals, and potential applications to satellite image processing (Section 4).

2. Data and methods

2.1 Satellite and *in situ* $R_{rs}(\lambda)$ matchups

The present study is based on satellite $R_{rs}(\lambda)$ spectra and concurrent *in situ* matchup measurements. There were 2540 and 3639 matchups extracted for SeaWiFS and MODISA, respectively, from the SeaWiFS Bio-optical Archive and Storage (SeaBASS) (Werdell and Bailey, 2005). A total of 2348 matchups were also assembled for VIIRS-SNPP, with the *in situ* and satellite $R_{rs}(\lambda)$ obtained from SeaBASS and NOAA CoastWatch, respectively. The $R_{rs}(\lambda)$ matchups were constructed in accordance with the availability of *in situ* data and the filtering criteria for satellite data (Bailey and Werdell, 2006; Mélin et al., 2011; Zibordi et al., 2009). First, the satellite data within a 5×5 pixel box centered at the *in situ* measurement location were considered. Second, the satellite data within the box were checked with the quality-flagging system (QFS), *l2_flags*: all pixels flagged as land, cloud, stray light, high glint, low radiance at 555 nm, high TOA radiance, or atmospheric correction failure were excluded from subsequent analysis. The third criterion applied was that at least 50% of the satellite pixels within the box are valid. Then, it was ensured that the solar zenith angle and sensor zenith angle are within 70° and 60°, respectively. The maximum time difference between satellite overpass and *in situ* sampling was set to ± 3 hours. The allowed maximum coefficient of variation of $R_{rs}(\lambda)$ inside the pixel box was by default 15%. To make sure of clear sky, the criterion for maximum difference between the *in situ* measured and modeled solar irradiance at sea surface is 20%. Figure 1 shows the geographic locations for the *in situ* and satellite matchups, most of which are located in nearshore regions with water depth shallower than 1000 m. We note that the 5×5 pixel box and the time interval of ± 3 hours are a compromise between the number of matchups and the quality of matchups determined for global waters by SeaBASS. Zibordi et al. (2009) and Mélin et al. (2011) recommended more restricted criteria with a 3×3 pixel box and a time interval of ± 2 hours for satellite validations in coastal waters. For the data sets used in this study, we tested the sensitivity of matchups to the different pixel boxes and time intervals but found negligible difference in the uncertainties of the resulted matchups. The criterion of ± 2 h time difference, however, reduced significantly the number of matchups by < ~10%. This observation justifies the use of the data filtering criteria of 5×5 pixels and ± 3 hours.

SeaWiFS and MODISA $R_{rs}(\lambda)$ data were generated with the *l2gen* package at the NASA Ocean Biology Processing Group (OBPG) during the latest reprocessing (R2018.0). The atmospheric correction was based on the classical scheme of Gordon and Wang (1994) and implemented with an iterative scheme to estimate the aerosol radiance at the NIR bands (Bailey et al., 2010). A total of 80 aerosol distributions were established and used during the processing

(Ahmad et al., 2010). The SeaWiFS $R_{rs}(\lambda)$ products have five bands centered at 412, 443, 490, 555, and 670 nm, while the MODISA $R_{rs}(\lambda)$ data have approximately the same nominal center wavelengths, including 412, 443, 488, 547, and 667 nm.

The VIIRS-SNPP $R_{rs}(\lambda)$ data were processed with the Multi-Sensor Level-1 to Level-2 (*MSL12*) ocean color data processing system at the NOAA Center for Satellite Applications and Research (STAR). *MSL12* is based on the NASA SeaWiFS Data Analysis System (SeaDAS) version 4.6 with modifications. Unlike SeaWiFS and MODISA processing, *MSL12* used the aerosol look-up table (LUT) of 12 aerosol models derived from Shettle and Fenn (1979). The VIIRS-SNPP $R_{rs}(\lambda)$ data were generated with the NIR-SWIR atmospheric correction algorithm (Wang, 2007; Wang and Shi, 2007; Wang et al., 2009). In addition, the algorithm of Wang and Jiang (2018) was used to estimate the blue-band $R_{rs}(\lambda)$ wherever $R_{rs}(410)$ is negative. The resultant VIIRS-SNPP $R_{rs}(\lambda)$ data have five wavelengths at 410, 443, 486, 551, and 671 nm; and no negative $R_{rs}(410)$ and $R_{rs}(443)$ values exist.

We computed the quality assurance (QA) scores for each of the satellite $R_{rs}(\lambda)$ spectra to quantitatively assess their data quality. The QA model (Wei et al., 2016b) was initially designed with nine visible bands, collectively representing the heritage and operational ocean color sensors. In the present study, we only considered the five "common" spectral bands centered around 412, 443, 488, 551, and 670 nm. As such, all the QA scores are distributed at six discrete levels of 0, 0.2, 0.4, 0.6, 0.8, and 1, with 1 representing the highest quality and 0 the lowest quality. Use of such common bands for the QA derivation facilitates the subsequent comparison of the obtained QA scores among different ocean color sensors. Recognizing the slight difference between three ocean color sensors' nominal center wavelengths and the five common bands of the QA model, we stress that this difference has a limited impact on the QA results. In Figure 2, we compare the frequency distribution of QA scores for three satellite sensors. According to the comparison, about 50% of satellite $R_{rs}(\lambda)$ data have the highest quality with QA = 1 and 30% of them show relatively good quality with QA = 0.8. The rest 20%, however, are found with lower quality scores (QA ≤ 0.6). In subsequent analysis, the satellite $R_{rs}(\lambda)$ data are divided into three subgroups: high-QA (QA ≥ 0.8), moderate-QA (0.4 ≤ QA ≤ 0.6), and low-QA (QA ≤ 0.2) data. The moderate- and low-QA data are the focus of our analysis.

2.2 Blue-band estimation algorithm

The blue-band estimation (BBE) algorithm consists of three components: a look-up table for the $R_{rs}(\lambda)$ spectral shapes, spectral matching, and spectral estimation. The three components are described in below with details.

(1) $R_{rs}(\lambda)$ spectral shapes

The $R_{rs}(\lambda)$ spectral shapes are represented by a total of 1768 normalized remote sensing reflectance spectra, $nR_{rs}(\lambda)$. These spectra were derived from hyperspectral $R_{rs}(\lambda)$ spectra (400–700 nm), which were originated from both *in situ* measurements and radiative transfer simulations. A description of the measurements and simulations can be found in Wei et al. (2016b) and Wei et al. (2019), respectively. The $R_{rs}(\lambda)$ spectra are representative of a wide range of waters with Chl varying from ~0.02 mg m^{-3} to > 50 mg m^{-3}. The hyperspectral $R_{rs}(\lambda)$ data were sub-sampled into five discrete bands at 412, 443, 488, 551, and 670 nm. The differences in the nominal center wavelengths among three sets of satellite $R_{rs}(\lambda)$ products are suppressed as they are not critical in the present context. The obtained five-band $R_{rs}(\lambda)$ spectra were then normalized by their respective root of the sum of squares (RSS), leading to

$$nR_{rs}(\lambda_i)=\frac{R_{rs}(\lambda_i)}{\left[\sum_{j=1}^{5}R_{rs}(\lambda_j)^2\right]^{1/2}},\ i = 1, 2, 3, 4 \text{ and } 5 \qquad (1)$$

where $nR_{rs}(\lambda)$ is dimensionless and the subscripts 1–5 correspond to the five bands from 412 nm to 670 nm. The $nR_{rs}(\lambda)$ spectra are characteristic of a few unique features. First, the $nR_{rs}(\lambda)$ spectral ratios at any two random bands remain the same with those of the corresponding $R_{rs}(\lambda)$ spectra. Second, the spectral curvature of $nR_{rs}(\lambda)$ remains unchanged in comparison to $R_{rs}(\lambda)$. Third, the magnitudes of $nR_{rs}(\lambda)$ always vary between 0 and 1. Last, the sum of squares of $nR_{rs}(\lambda)$ at all five bands is equal to 1. In this context, these $nR_{rs}(\lambda)$ spectra describe the spectral shapes for the corresponding $R_{rs}(\lambda)$ spectra.

In Figure 3, we illustrate the range of variation of the spectral values at 41x and 443 nm and related spectral ratios for the normalized reflectance of the LUT (denoted $nR_{rs}^{lut}(\lambda)$) and those for the *in situ* data concurrent with satellite overpass. The evaluation data and the LUT exhibit a very similar pattern of variation, with the latter spanning over a slightly wider range. Most of the evaluation data have nR_{rs}(41x) and nR_{rs}(443) lower than 0.7 and 0.6, respectively. The nR_{rs}(41x)/nR_{rs}(443) and nR_{rs}(443)/nR_{rs}(55x) ratios of the evaluation data are confined within a much narrower domain (0.6–1.1 and 0.2–1.1, respectively) than the LUT. Outliers do exist, particularly for the SeaWiFS matchup data. Overall, the range of variation of all data sets shown in Figure 3 is about the same as that of the compiled data in Valente et al. (2016).

(2) Spectral matching

For a satellite $R_{rs}(\lambda)$ spectrum in question, the first step is to determine a “true” spectral shape as a reference. For this purpose, we take advantage of the fact that satellite R_{rs}(48x) and R_{rs}(55x) measurements usually have good quality (Antoine et al., 2008; Hlaing et al., 2013; Zibordi et al., 2009). The R_{rs}(67x) data are sometimes subjected to large uncertainties, but their impact on the model performance is limited; we will discuss this problem in the sensitivity analysis in Section 3.4. As such, the satellite R_{rs}(48x), R_{rs}(55x), and R_{rs}(67x) can be used as a basis for further processing. First, following the spectral angle mapper (SAM) (Kruse et al., 1993), we quantify the spectral similarity between satellite-derived R_{rs}(48x), R_{rs}(55x), and R_{rs}(67x) values and each of the $nR_{rs}^{lut}(\lambda)$ spectra by the cosine distance

$$d = 1 - \frac{\sum_{i=3}^{5}\left[nR_{rs}^{lut}(\lambda_i) \cdot R_{rs}(\lambda_i)\right]}{\sqrt{\sum_{i=3}^{5}\left[nR_{rs}^{lut}(\lambda_i)\right]^2 \sum_{i=3}^{5}\left[R_{rs}(\lambda_i)\right]^2}} \tag{2}$$

where d is the cosine distance between the vectors of $nR_{rs}^{lut}(\lambda)$ and satellite $R_{rs}(\lambda)$ at 48x, 55x, and 67x nm bands. Second, we search for the minimum d and locate the corresponding $nR_{rs}^{lut}(\lambda)$ spectrum from the LUT. Such selected $nR_{rs}^{lut}(\lambda)$ spectrum is regarded as the spectral shape for the satellite $R_{rs}(\lambda)$ in question.

(3) Spectral estimation

According to Eq. (1), the satellite R_{rs}(41x) and R_{rs}(443) in question can be normalized as below

$$\begin{cases} \dfrac{R_{rs}(41\mathrm{x})}{\left[R_{rs}(41\mathrm{x})^2 + R_{rs}(443)^2 + R_{rs}(48\mathrm{x})^2 + R_{rs}(55\mathrm{x})^2 + R_{rs}(67\mathrm{x})^2\right]^{1/2}} = nR_{rs}(41\mathrm{x}) \\ \dfrac{R_{rs}(443)}{\left[R_{rs}(41\mathrm{x})^2 + R_{rs}(443)^2 + R_{rs}(48\mathrm{x})^2 + R_{rs}(55\mathrm{x})^2 + R_{rs}(67\mathrm{x})^2\right]^{1/2}} = nR_{rs}(443) \end{cases} \tag{3}$$

where R_{rs}(41x), R_{rs}(443), nR_{rs}(41x), and nR_{rs}(443) are unknown. Since we have determined the spectral shape through spectral matching, we substitute nR_{rs}(41x) and nR_{rs}(443) in Eq. (3) with $nR_{rs}^{lut}(412)$ and $nR_{rs}^{lut}(443)$, respectively. As a result, Eq. (3) can be rewritten as

$$\begin{cases} R_{rs}(41\mathrm{x}) = \left[\dfrac{R_{rs}(48\mathrm{x})^2 + R_{rs}(55\mathrm{x})^2 + R_{rs}(67\mathrm{x})^2}{nR_{rs}^{lut}(488)^2 + nR_{rs}^{lut}(551)^2 + nR_{rs}^{lut}(670)^2} \right]^{1/2} \times nR_{rs}^{lut}(412) \\ R_{rs}(443) = \left[\dfrac{R_{rs}(48\mathrm{x})^2 + R_{rs}(55\mathrm{x})^2 + R_{rs}(67\mathrm{x})^2}{nR_{rs}^{lut}(488)^2 + nR_{rs}^{lut}(551)^2 + nR_{rs}^{lut}(670)^2} \right]^{1/2} \times nR_{rs}^{lut}(443) \end{cases} \tag{4}$$

where $R_{rs}(41\mathrm{x})$ and $R_{rs}(443)$ are estimated by both satellite $R_{rs}(\lambda)$ data at the three bands of 48x, 55x, and 67x nm and $nR_{rs}^{lut}(\lambda)$ data.

2.3 Metrics for uncertainty evaluation

The relative difference (ε) was computed to assess the uncertainty of satellite products including $R_{rs}(\lambda)$ spectral values at 41x, 443, 48x, 55x, and 67x nm, and the $R_{rs}(\lambda)$ spectral ratios at 41x and 443 nm band, i.e., $R_{443}^{41\mathrm{x}}$, and the ratios at 443 and 55x nm, i.e., $R_{55\mathrm{x}}^{443}$, as

$$\varepsilon = \frac{S_1 - S_2}{S_2} \times 100\% \ , \tag{5}$$

where S_1 and S_2 refer to the satellite-derived values and the corresponding *in situ* values, respectively. The median of the relative difference ($\bar{\varepsilon}$) or bias was derived as

$$\bar{\varepsilon} = median\left\{ \frac{S_1 - S_2}{S_2} \right\} \times 100\% \ . \tag{6}$$

Further, we derived the absolute percentage difference (APD, denoted as $|\bar{\varepsilon}|$) as

$$|\bar{\varepsilon}| = median\left\{ \left| \frac{S_1 - S_2}{S_2} \right| \right\} \times 100\% \ . \tag{7}$$

The root-mean-square deviation (RMSD) was also computed to assess the accuracy of satellite products, as

$$RMSD = \sqrt{\frac{1}{N} \sum_{i=1}^{N} \left(S_{i,1} - S_{i,2} \right)^2} \ . \tag{8}$$

In analogy to $\bar{\varepsilon}$, the unbiased relative difference (denoted as $\bar{\phi}$) was calculated as,

$$\bar{\phi} = \frac{2}{N}\sum_{i=1}^{N}\frac{S_{i,1} - S_{i,2}}{S_{i,1} + S_{i,2}} \times 100\% \quad , \tag{9}$$

where $S_{i,1}$ and $S_{i,2}$ are the inherent optical properties derived from the satellite $R_{rs}(\lambda)$ data and *in situ* $R_{rs}(\lambda)$ matchup data. The unbiased absolute percentage difference (UPD, denoted as $|\bar{\phi}|$) was

$$|\bar{\phi}| = \frac{2}{N}\sum_{i=1}^{N}\left|\frac{S_{i,1} - S_{i,2}}{S_{i,1} + S_{i,2}}\right| \times 100\% \quad . \tag{10}$$

2.4 Sensitivity analysis

The sensitivity of R_{rs}(41x) and R_{rs}(443) estimation to the uncertainties of the algorithm input values of R_{rs}(48x), R_{rs}(55x), and R_{rs}(67x) was assessed with the IOCCG (2006) synthetic $R_{rs}(\lambda)$ data after adding uncertainties to R_{rs}(48x), R_{rs}(55x), and R_{rs}(67x). The hyperspectral $R_{rs}(\lambda)$ data of IOCCG (2006) were first sampled at 412, 443, 488, 551, and 670 nm. The resultant multiband $R_{rs}(\lambda)$ spectra were then clustered based on the cosine distance as quantified by Eq. (2). To simplify, we assumed three classes to represent these spectra (Classes-1, -2, and -3). As shown in Figure 4, each of three classes is characteristic of a distinctive spectral shape, roughly corresponding to blue, blue-green, and green-yellow colors. For Class-1 water, the maximum spectral values are often present in the blue bands, while R_{rs}(670) is usually very small. In terms of the trophic status, Class-1 is found with low Chl of 0.03–0.7 mg m^{-3} (0.14 mg m^{-3} on average). Class-2 water is characteristic of moderate R_{rs}(412) and R_{rs}(670) values, and generally of moderate Chl, ranging from 0.3 to 10.0 mg m^{-3} (1.6 mg m^{-3} on average). Class-3 waters are representative of relatively turbid environments, with high R_{rs}(670) but relatively small R_{rs}(412) values, where Chl are high, varying from 1.5 to 30.0 mg m^{-3} (15 mg m^{-3} on average).

In the following, the $R_{rs}(\lambda)$ spectra within each of three classes were used to synthesize error-disturbed reflectance, $\tilde{R}_{rs}(\lambda)$. We investigated a simplified situation where only one of $R_{rs}(488)$, $R_{rs}(551)$, or $R_{rs}(670)$ values was subjected to uncertainty, while the other two were error-free. The error-disturbed $\tilde{R}_{rs}(\lambda)$ value was simulated as below

$$\tilde{R}_{rs}(\lambda_i) = R_{rs}(\lambda_i)\times\left(1+2\boldsymbol{\varepsilon}\cdot\Re\right) \tag{11}$$

where λ_i refers to 488, 551, or 670 nm, ε is the relative error varying from −50% to 50% (with a 5% step), and $\Re$ is a random value between 0 and 1. For each ε, Eq. (11) was repeated 100 times, leading to a total of 17300, 13700, and 19000 error-disturbed $\tilde{R}_{rs}(\lambda_i)$ values for Classes-1, -2, and -3, respectively. From these synthetic reflectance, new $R_{rs}(412)$ and $R_{rs}(443)$ values were estimated with the BBE algorithm and then compared with known values to quantify their difference.

It is noted that the uncertainty of satellite-derived $R_{rs}(\lambda)$ products remains difficult to characterize as it is not only spectrally variable but dependent on environmental conditions as well as instrumental calibration (Antoine et al., 2008; Hu et al., 2013; Wei et al., 2018). To gain further perspective, we considered four simplistic scenarios with different combinations of uncertainties simultaneously assigned to $R_{rs}(488)$, $R_{rs}(551)$, and $R_{rs}(670)$. Table 1 lists the amplitudes of the absolute percentage errors commonly observed in the ocean color satellite $R_{rs}(\lambda)$ products (Antoine et al., 2008; Hlaing et al., 2013; Zibordi et al., 2009). In addition, we also considered a particular scenario with zero uncertainty for the purpose of comparison. The following model was used to create error-disturbed $\tilde{R}_{rs}(\lambda)$ at 488, 551, and 670 nm,

$$\tilde{R}_{rs}(488,551,670) = R_{rs}(488,551,670)\cdot\left[1+2\left(2\Re-1\right)\cdot|\bar{\varepsilon}|_{488,551,670}\right] \tag{12}$$

where $|\bar{\varepsilon}|_{488,551,670}$ refers to the absolute percentage errors at 488, 551, and 670 nm in Table 1 and

$\Re$ is a random number between 0 and 1. Eq. (12) predicts spectrally coherent uncertainties, where the relative errors share the same positive or negative signs at 488, 551, and 670 nm. As the above, Eq. (12) was repeated 100 times for each $R_{rs}(\lambda)$ spectrum within each water class to generate the corresponding $\tilde{R}_{rs}(\lambda)$ values.

3. Results

3.1 Comparison of satellite and *in situ* $R_{rs}(\lambda)$ matchups

We first assessed the satellite R_{rs}(48x), R_{rs}(55x), and R_{rs}(67x) uncertainties based on the satellite and *in situ* matchups as the $R_{rs}(\lambda)$ data quality at these three bands is important for the implementation of the BBE algorithm. Comparisons of three groups of analyses in Table 2 indicate that the satellite R_{rs}(48x), R_{rs}(55x), and R_{rs}(67x) are prone to increasingly larger uncertainties with the decrease of QA scores, and *vice versa*. For the high-QA satellite data, specifically, R_{rs}(48x) and R_{rs}(55x) only suffer an absolute relative difference of 10%–13% and a negative bias varying between 0% and −10%. Even at the red band of 67x nm, the analyses show a fairly small uncertainty for the reflectance values, with $|\varepsilon|$ varying between 11% and 22% and $\overline{\varepsilon}$ between −16% and 2%. In comparison to high-QA data, the moderate-QA group has much fewer data points. Also, R_{rs}(48x), R_{rs}(55x), and R_{rs}(67x) measurements in this group are found with increased uncertainties, particularly for $|\varepsilon|$. The low-QA group only accounts for a very small portion of the satellite measurements used herein. Their R_{rs}(48x), R_{rs}(55x), and R_{rs}(67x) measurements are susceptible to almost doubled relative differences (with $|\varepsilon|$ up to 45%) and biases (with $\overline{\varepsilon}$ beyond −44%), in comparison to the high-QA group.

Similar to R_{rs}(48x), R_{rs}(55x), and R_{rs}(67x), the uncertainties of satellite R_{rs}(41x) and R_{rs}(443) are also found to increase with decreasing QA scores (Table 3). Taking MODISA as an example, the $R_{rs}(412)$ uncertainty increased from $|\bar{\varepsilon}|$ = 27% in high-QA group to $|\bar{\varepsilon}|$ = 51% for moderate-QA group, and finally to $|\bar{\varepsilon}|$ = 89% for low-QA data. It is also noted that many SeaWiFS and MODISA $R_{rs}(412)$ values in these datasets are negative, but it is rare to observe negative $R_{rs}(410)$ values for VIIRS-SNPP due to a recent improvement made by Wang and Jiang (2018). Exclusion of these negative R_{rs}(41x) data from evaluation, however, has resulted in a significant reduction in the total numbers of available matchups for R_{rs}(41x). Particularly for SeaWiFS and MODISA, the numbers of $R_{rs}(412)$ matchups for moderate- and low-QA subgroups are about 15%–30% less than $R_{rs}(443)$. The uncertainties of satellite R_{rs}(41x) and $R_{rs}(443)$ are generally greater than the corresponding R_{rs}(48x) and R_{rs}(55x), which is consistent with earlier analyses (Hlaing et al., 2013; Qin et al., 2017; Zibordi et al., 2009). This feature can be partly attributable to the relatively small values of R_{rs}(41x) and $R_{rs}(443)$ in the evaluation data, and partly to the relatively large uncertainty of *in situ* measurements at these two bands in coastal waters (also see Hooker et al., 2002).

The correspondence between increasing uncertainties and decreasing QA scores for satellite $R_{rs}(\lambda)$ measurements has several implications. Firstly, it provides a first-hand evidence that the QA scores are a useful measure of the overall data quality for satellite-derived $R_{rs}(\lambda)$ spectra. Secondly, it is important to note that the satellite validation analyses (e.g., Hlaing et al., 2013; Qin et al., 2017; Wei et al., 2018) tend to consider all available matchups as a whole, in which the satellite $R_{rs}(\lambda)$ spectra with different QA scores are mixed. Since the moderate- and low-QA score data often account for a relatively small percentage of the available data (see Figure 2), their relatively larger uncertainties are often suppressed and less likely to dominate the overall uncertainty. The above analyses provided a feasible way to identify specific subgroups of the satellite $R_{rs}(\lambda)$ measurements based on their QA scores.

3.2 Estimated R_{rs}(41x) and R_{rs}(443)

The evaluation results for BBE-estimated R_{rs}(41x) and R_{rs}(443) are also included in Table 3 for direct comparison with the original satellite products. Notably, all those initially negative R_{rs}(41x) and R_{rs}(443) values for SeaWiFS and MODISA are now restored to positive values, leading to a significant increase in the total number of utilizable R_{rs}(41x) and R_{rs}(443) data. The larger numbers of positive R_{rs}(41x) values could enhance the effectiveness of subsequent bio-optical retrievals as many semi-analytical inversion algorithms (Carder et al., 1999; Lee et al., 2002; Wei and Lee, 2015; Werdell et al., 2013) require R_{rs}(410) or R_{rs}(412) as input to separate phytoplankton and CDOM, which will be discussed later in Section 4. Partly because of the change of the number of observations, however, the BBE-estimated R_{rs}(412) for SeaWiFS did not show a reduction in its uncertainties, rather experienced some degree of increase in $|\bar{\varepsilon}|$, from 22% to 36% for the moderate-QA group. In comparison to MODISA, the estimated R_{rs}(412) data exhibited a slight increase in the biases ($\bar{\varepsilon}$ increased from −6% to −8% for moderate-QA group); this is to a large degree a result of the large biases associated with R_{rs}(488), R_{rs}(547), and R_{rs}(667) (Table 2). On the other hand, without much change to the total number of the VIIRS-SNPP observations, the estimated R_{rs}(410) and R_{rs}(443) data show much reduced uncertainties for both moderate- and low-QA groups. Overall, very limited improvements were found for the high-QA data of three satellites. This phenomenon may be further explained from the following two perspectives. First, the high QA scores imply that the R_{rs} spectra are already of high quality. Estimations with the BBE algorithm may thus be superfluous for high-QA data. Second, part of the normalized remote sensing reflectance spectra within the LUT are also used by the QA model (Wei et al., 2016b); it is technically difficult to further improve the spectral shapes of satellite $R_{rs}(\lambda)$ data by the BBE algorithm. As a matter of fact, as indicated in Table 3, the original high-QA satellite data appear most accurate. They will less likely benefit from an estimation scheme as developed here.

To further highlight the model performance, we contrasted the satellite R_{rs}(41x) and R_{rs}(443) with *in situ* matchups for the moderate-QA group of data in scatterplots (Figure 5), with the BBE-estimated R_{rs}(41x) and R_{rs}(443) overlaid for comparison. Note that these illustrations have included all available matchup data in this subgroup, including positive and negative values. As shown in the plots, many SeaWiFS and MODISA R_{rs}(412) values are negative, and even some of the corresponding R_{rs}(443) data are negative as well. Unlike SeaWiFS and MODISA, the BBE estimates of R_{rs}(412) and R_{rs}(443) are all physically meaningful values. The estimated R_{rs}(412) and R_{rs}(443) are distributed much more tightly around the 1:1 line than the original satellite data (for SeaWiFS, MODISA, and VIIRS-SNPP). As a result, the linear regression slopes for the BBE estimates and the *in situ* matchups are generally much closer to unity.

3.3 $R_{rs}(\lambda)$ spectral ratios

Since the BBE algorithm is based on the knowledge of the $R_{rs}(\lambda)$ spectral shapes, it is expected that such estimated R_{rs}(41x) and R_{rs}(443) should yield improvement on the $R_{rs}(\lambda)$ spectral ratios. We derived the ratios of R_{rs}(443) to R_{rs}(55x) and R_{rs}(41x) to R_{rs}(443) and compared them with those of *in situ* matchup data in Table 4. Among three subgroups of data, very limited differences are observed in R_{443}^{41x} and R_{55x}^{443} for the high-QA group, which is consistent with the analyses of R_{rs}(41x) and R_{rs}(443) uncertainties in Table 3. For the moderate-QA data, the presence of many negative R_{rs}(41x) and R_{rs}(443) data have resulted in either negative R_{443}^{412} or sometimes positive outliers and some negative R_{55x}^{443} values (see scatterplots in Figure 6). The

BBE algorithm improved both R^{41x}_{443} and R^{443}_{55x} with overall reduced uncertainties and significantly increased the number of utilizable data (by as much as ~20% for the moderate-QA data). The improvement in the spectral band ratios, along with estimated spectral values, is important for bio-optical inversion, in that they are indispensable for many empirical ocean color algorithms (Morel and Gentili, 2009; O'Reilly et al., 1998) and semi-analytical algorithms (IOCCG, 2006; Werdell et al., 2018). We will discuss the potential impact on bio-optical retrievals in Section 4.3.

3.4 Sensitivity of R_{rs}(41x) and R_{rs}(443) estimation

The sensitivity of R_{rs}(41x) and R_{rs}(443) estimation to the input $R_{rs}(\lambda)$ values at 48x, 55x, or 67x nm is illustrated in Figure 7. Several important conclusions can be readily reached from the comparisons. First, the minimum uncertainty of estimated R_{rs}(41x) and R_{rs}(443) ($|\bar{\varepsilon}| \approx 15\%$) is observable with error-free input $R_{rs}(\lambda)$ data for all classes of waters, which can be considered as the inherent uncertainty for the BBE algorithm. Second, it is found that the estimations for R_{rs}(41x) and R_{rs}(443) are most sensitive to the uncertainty of R_{rs}(48x). For instance, when R_{rs}(48x) has $\varepsilon = 30\%$, the BBE-estimated R_{rs}(41x) can be subjected to an uncertainty as large as $|\bar{\varepsilon}| = 50\%$–$60\%$ over three classes of waters. The uncertainty of input R_{rs}(55x) plays a secondary role; according to our analysis, an error of $\varepsilon = 30\%$ with R_{rs}(55x) will result in a smaller uncertainty for R_{rs}(41x), with $|\bar{\varepsilon}|$ less than 35%. In contrast, the uncertainty of R_{rs}(67x) appears to be the least important element to influence the R_{rs}(41x) and R_{rs}(443) uncertainties.

The above-revealed differential dependency of the algorithm uncertainty on specific wavelengths can be explained by the uncertainty propagation of the BBE algorithm. In Eq. (13), the uncertainty of R_{rs}(41x) is expressed as a function of the input $R_{rs}(\lambda)$ and $nR^{lut}_{rs}(\lambda)$ values and the associated uncertainty at a specific band λ_j (48x, 55x, or 67x nm), following the principle of uncertainty propagation,

$$u(41\text{x}) = \frac{1}{\sqrt{R_{rs}(48\text{x})^2 + R_{rs}(55\text{x})^2 + R_{rs}(67\text{x})^2}} \cdot R_{rs}(\lambda_j) \cdot u(\lambda_j) \cdot \frac{nR_{rs}^{lut}(412)}{\sqrt{nR_{rs}^{lut}(488)^2 + nR_{rs}^{lut}(551)^2 + nR_{rs}^{lut}(670)^2}} \tag{13}$$

In Eq. (13), we assumed zero uncertainty for $nR_{rs}^{lut}(\lambda)$ and uncorrelated input quantities. As the two fractional terms in Eq. (13) are certain for a given satellite reflectance spectrum, u(41x) is sensitive to the input value for $R_{rs}(\lambda_j)$ and associated uncertainty $u(\lambda_j)$. Recalling Figure 4, R_{rs}(67x) are usually smaller than R_{rs}(48x) and/or R_{rs}(55x) in the test data, the uncertainty propagation of the R_{rs}(67x) uncertainty to the total uncertainty is thus relatively less critical. In extremely turbid waters, the R_{rs}(67x) values can be very large; but the corresponding uncertainties tend to be small. For Class-1 waters, R_{rs}(48x) are almost always higher than R_{rs}(55x), thus playing a dominant role in the resulted R_{rs}(41x) and R_{rs}(443). For Class-2 waters, there are some instances where R_{rs}(55x) are comparable to or even higher than R_{rs}(48x); under these situations, R_{rs}(55x) may play a more important role (e.g., Figure 7c). Based on this analysis, the BBE algorithm may be applicable to a wide range of environments.

According to the five combinations of uncertainties (Table 1), the increase of the uncertainties in input $R_{rs}(\lambda)$ leads to increased uncertainties in estimated R_{rs}(41x) and R_{rs}(443) (Table 5). In particular, the absolute percentage differences for R_{rs}(41x) herein experienced a huge jump, from 9% to 56%. But, recall that the $|\bar{\varepsilon}|$ for moderate-QA satellite R_{rs}(48x) and R_{rs}(55x) data are generally between 12% and 23% (Table 2). That is to say, the simulation No. 3 best describes the realistic situations, in which the $|\bar{\varepsilon}|$ for estimated R_{rs}(41x) varies between 25% and 37%, a range close to the evaluation results in Table 3. Besides, our analyses indicate a weak dependency of

R_{rs}(41x) uncertainty on the class of water. The BBE algorithm tends to bias the estimation of R_{rs}(41x) and R_{rs}(443) for Class-3, for which the nR_{rs}(41x) and nR_{rs}(443) values are often relatively smaller (recall Figure 4).

4. Discussion

4.1 Why the algorithm works

The BBE algorithm infers the $R_{rs}(\lambda)$ spectral shapes through a spectral matching procedure using initial satellite $R_{rs}(\lambda)$ values measured at 48x, 55x, and 67x nm and subsequently estimates R_{rs}(41x) and R_{rs}(443). It is based on an implicit assumption that the normalized satellite $R_{rs}(\lambda)$ values at 41x and 443 nm are approximately equal to those selected from the LUT after the spectral matching. According to the validation results, this assumption is reliable for the estimation of $R_{rs}(\lambda)$ at blue bands. The algorithm's success benefits from the following two facts. First, the R_{rs}(48x) and R_{rs}(55x) values generated from satellites are relatively accurate (Table 2) (also see Antoine et al., 2008; Hlaing et al., 2013; Qin et al., 2017; Zibordi et al., 2009). Second, the algorithm remains least sensitive to R_{rs}(67x) for most waters (Figure 7). These factors favor and facilitate the optimal performance of the BBE algorithm.

The light absorption and scattering properties of optically active constituents determine the $R_{rs}(\lambda)$ spectra, simplified as the following (Gordon et al., 1988),

$$R_{rs}(\lambda) \propto \frac{b_{bp}(\lambda) + b_{bw}(\lambda)}{a_{ph}(\lambda) + a_{dg}(\lambda) + a_{w}(\lambda) + b_{bp}(\lambda) + b_{bw}(\lambda)} \tag{14}$$

where $b_{bp}(\lambda)$ and $b_{bw}(\lambda)$ are the scattering coefficients due to particulates and pure seawater, respectively; $a_{ph}(\lambda)$, $a_{dg}(\lambda)$ and $a_{w}(\lambda)$ refer to the absorption coefficients of phytoplankton, colored detrital material (including CDOM and detritus), and pure seawater, respectively; and,

$a_w(\lambda)$ and $b_{bw}(\lambda)$ are often taken as wavelength-specific constants (Lee et al., 2015b; Mason et al., 2016; Zhang and Hu, 2009). Among all these inherent optical properties (IOPs), the $b_{bp}(\lambda)$ spectrum is monotonous under most circumstances and can be described by a power-law function. Thus, the spectral variability of $R_{rs}(\lambda)$ is mostly dominated by light absorption spectra. The light absorption of phytoplankton is contributed by various pigments (Bricaud et al., 1995; Bricaud et al., 2004). In the visible domain, $a_{ph}(\lambda)$ values are spectrally interdependent (Bricaud et al., 1998; Lee et al., 1998; Sathyendranath et al., 1987). Further, the light absorption of colored detrital material is also spectrally dependent and can be simplified by an exponential decay model. Given the spectral dependency of IOPs, R_{rs}(48x), R_{rs}(55x), and R_{rs}(67x) values are as a matter of fact interconnected with R_{rs}(41x) and R_{rs}(443). This is the basis on which R_{rs}(41x) and R_{rs}(443) can be estimated from Eq. (14). The accuracy of model estimation will primarily depend on the degree of our understanding of the IOPs and the IOP-R_{rs} relationships.

4.2 Algorithm limitations

We reiterate that the BBE algorithm is by no means intended to replace the measurements of R_{rs}(41x) and R_{rs}(443) from satellite ocean color sensors. Rather, it provides a workaround to estimate R_{rs}(41x) and R_{rs}(443) when the satellite-derived $R_{rs}(\lambda)$ spectra are highly questionable and are almost useless in blue bands. Like other remote sensing algorithms, the BBE algorithm is subject to uncertainties and limitations. Fully understanding the estimation uncertainty will require advanced statistical methodologies (Jay et al., 2018; Wang et al., 2005) and knowledge of the satellite $R_{rs}(\lambda)$ uncertainty in various waters (e.g., Hu et al., 2013). According to our preliminary analyses, the error propagation from R_{rs}(48x), R_{rs}(55x), and R_{rs}(67x) can be a primary source of uncertainty for model-estimated R_{rs}(41x) and R_{rs}(443). Besides, a few other contributing factors merit further discussion. First, the proposed spectral matching procedure uses the reflectance at three base wavelengths of 48x, 55x, and 67x nm. The use of a subset of wavelengths for water optical classification may introduce uncertainties, which further propagate to the estimation of the $R_{rs}(\lambda)$ spectral shapes, and finally to the estimated R_{rs}(41x) and R_{rs}(443). The results in Figure 7 and Table 5 are based upon the IOCCG (2006) data, which are well represented by the LUT. The uncertainties ($|\varepsilon| \leq 13\%$, $-10\% \leq \varepsilon \leq 1\%$, and $0.0004 < \mathrm{RMSD} < 0.002\ \mathrm{sr}^{-1}$) derived with error-free R_{rs}(48x), R_{rs}(55x), and R_{rs}(67x) are basically equivalent to the algorithm residual uncertainties originated from the use of three-band reflectance. Second, it is difficult (if not impossible) for the LUT to characterize all $R_{rs}(\lambda)$ spectral shapes occurring in natural waters. In spite of the satisfactory validation results presented herein, there might exist peculiar waters not represented by the current LUT. Thus, it is necessary to continue to enrich the LUT towards a universal application. Third, the $R_{rs}(\lambda)$ spectrum is determined by the water IOPs including the spectral slope (S_{dg}) for $a_{dg}(\lambda)$. Variation of S_{dg} alone can cause substantial variability for $R_{rs}(\lambda)$ in short blue bands (Wei et al., 2016a), in which case the estimation of R_{rs}(41x) and R_{rs}(443) will suffer from uncertainty. Lastly, the BBE algorithm has simplified the spectral settings to five common bands (412, 443, 488, 551, and 670 nm), which ignored the discrepancy of center wavelengths among SeaWiFS, MODISA, and VIIRS-SNPP. Based on IOCCG (2006) data, we evaluated the potential impact on $R_{rs}(\lambda)$ values due to this ignorance. Comparing with the common bands, the R_{rs}(41x), R_{rs}(48x), R_{rs}(55x), and R_{rs}(67x) are subject to relatively small differences, with $|\varepsilon|$ = 1.1%, 1.7%, 4%, and 3.6%, respectively. These uncertainties are much smaller than the inherent uncertainties of the BBE algorithm and/or those from measurements, thus not important in this context. Although IOCCG synthetic data are not inclusive of every types of waters in nature, the uncertainty analysis based on them should provide a representative assessment. The algorithm uncertainty can be further explored when the uncertainty of satellite-derived $R_{rs}(\lambda)$ spectra is better known.

4.3 Potential improvement on bio-optical retrievals

The primary purpose of maintaining high-quality satellite $R_{rs}(\lambda)$ measurements is to provide the aquatic science community with reliable bio-optical retrievals. To demonstrate the contributions of the algorithm, we derived $a_{ph}(443)$ and $a_{dg}(443)$ from the original satellite $R_{rs}(\lambda)$ data, estimated $R_{rs}(\lambda)$ data at blue bands, and *in situ* $R_{rs}(\lambda)$ matchups, using the quasi-analytical algorithm (QAA) (Lee et al., 2002). According to the results of uncertainty analysis (Table 6), the implementation of the BBE algorithm has exerted negligible impacts on the $a_{ph}(443)$ and $a_{dg}(443)$ retrievals for the high-QA satellite data. This is consistent with the observation in Section 3 in which the BBE algorithm was shown unable to make substantial improvements to $R_{rs}(41x)$ and $R_{rs}(443)$ for the high-QA satellite data (Table 3). For the moderate-QA data, the retrievals of $a_{dg}(443)$ from BBE-estimated R_{rs} spectra are much more accurate than those from the original satellite $R_{rs}(\lambda)$ data (except for SeaWiFS), with much reduced $|\bar{\Phi}|$, $\bar{\Phi}$, and RMSD. Also inspiringly, the total number of valid $a_{ph}(443)$ and $a_{dg}(443)$ retrievals from SeaWiFS and MODISA are increased by as much as 15%–30%. This improvement is significant as accurate, and potentially more representative, data points will be accounted for in relevant ocean color applications. Similar increases in the number of bio-optical products and decreases in $a_{dg}(443)$ uncertainty are also found in the low-QA SeaWiFS and MODISA data. In contrast, no significant change in the total numbers of $a_{ph}(443)$ and $a_{dg}(443)$ retrievals are observed for VIIRS-SNPP, mostly because VIIRS-SNPP has nearly no negative $R_{rs}(410)$ or $R_{rs}(443)$ values (see Figure 5 and Figure 6).

4.4 Condition of applicability

It is important to understand the condition of applicability under which the BBE algorithm can be best used to estimate $R_{rs}(41x)$ and $R_{rs}(443)$. The quality flagging system is the quality-control measure adopted by space agencies like NASA and NOAA to generate scientific quality data (Bailey and Werdell, 2006; Mikelsons et al., 2020). In practice, the often-used filtering flags include land, cloud, stray light, high glint, low radiance at 55x nm, high TOA radiance, and atmospheric correction failure, etc. The pixels passing the flag check will be regarded as good quality and included in the higher-level products. The satellite $R_{rs}(\lambda)$ data used for our analyses have been checked for valid quality flags also. The QA scoring system (Wei et al., 2016b) is a quantitative measure for the quality of each $R_{rs}(\lambda)$ spectrum, which can further help to identify questionable data. The present study has considered both the flags and the QA scores. According to Figure 2, about 20% of the satellite data available for validation analysis, which have passed the quality flag filtering, are found to have moderate- or low-QA scores ($QA \leq 0.6$). This portion of satellite $R_{rs}(\lambda)$ spectra is characteristic of high uncertainties and can be further improved by the BBE algorithm. In Figure 8, we illustrate the percentage of moderate- and low-QA satellite $R_{rs}(\lambda)$ in the U.S. coastal and inland waters. Within each plot, the pixels have passed the quality flag filtering. Obviously, the “correctable” satellite $R_{rs}(\lambda)$ products are mostly found in the nearshore waters, where the atmospheric conditions and water optical properties are most likely complex. Despite the positive results (Table 3 and Table 4), it is without doubt that estimating $R_{rs}(41x)$ and $R_{rs}(443)$ with the BBE algorithm in such complex waters can sometimes be challenging, especially when the LUT does not sufficiently characterize the complex water optical variations. There is a continuous need for accumulation and inclusion of representative *in situ* $R_{rs}(\lambda)$ spectra in the LUT.

4.5 Satellite ocean color image processing

The coastal waters are typical of high absorption and scattering properties, with non-negligible water-leaving radiance at the NIR bands (Siegel et al., 2000; Wang and Shi, 2005). Close to sources of air pollutions, the types of aerosols are complex and more difficult to predict (IOCCG, 2010). The oceanic and atmospheric conditions together render a very critical situation for atmospheric correction. Here, we used an imagery of the northern Gulf of Mexico captured by VIIRS-SNPP to demonstrate the BBE algorithm performance. As shown in Figure 9a, the original image was processed with the latest *MSL12* ocean color data processing system, which incorporated the Wang and Jiang (2018) algorithm. It is shown that the $R_{rs}(410)$ values are extremely low in the northern shelf waters, many of which are infinitesimally close to zero. According to the quality flags, there possibly existed strongly absorbing aerosols over a great number of pixels in these waters (highlighted by the dashed line in Figure 9a). To implement the BBE algorithm, all the pixels were first subjected to the quality check for land, cloud, stray light, high glint, and high TOA, etc. Then, the moderate- and low-QA pixels were identified and finally $R_{rs}(410)$ and $R_{rs}(443)$ were estimated with the proposed algorithm. The new $R_{rs}(410)$ image is presented in Figure 9b, which includes the model-estimated $R_{rs}(410)$ values at low- and moderate-QA pixels and the original values at high-QA pixels. It is obvious that the close-to-zero pixels are rectified to much larger values; some originally higher $R_{rs}(410)$ values are decreased. As a result, the estimated $R_{rs}(410)$ image over the Mississippi Delta waters has shown characteristics of spatial pattern with realistic gradients and amplitudes.

5. Conclusions

Accurate retrieval of remote sensing reflectance in the two short blue bands of 41x nm and 443 nm in coastal and inland waters from ocean color satellites has been a challenge because of the complex oceanic and atmospheric properties. Whereas great effort has been put in, a considerable proportion of satellite reflectance products are still found susceptible to large uncertainties. In this study, we developed a spectral shape based algorithm to estimate R_{rs}(41x) and R_{rs}(443). The algorithm uses a spectral-matching procedure to determine the spectral shapes for the satellite $R_{rs}(\lambda)$ spectra in question based on the initial satellite $R_{rs}(\lambda)$ measurements at the three wavelengths of 48x, 55x, and 67x. This is a novel attempt to complement and enhance the existing efforts for atmospheric correction. Evaluation with satellite (SeaWiFS, MODISA, and VIIRS-SNPP) and *in situ* $R_{rs}(\lambda)$ matchups in global oceans, with most of the data located within coastal waters, shows that the estimated R_{rs}(41x) and R_{rs}(443) have much-reduced uncertainties with respect to the initial satellite data. It can be expected that such estimated R_{rs}(41x) and R_{rs}(443) data will enhance the quality of bio-optical retrievals for the absorption coefficients of phytoplankton and CDOM and detritus, and increase the quantities of utilizable bio-optical products. Despite the inherent uncertainty (~10%), the algorithm is shown to be applicable to a wide range of waters. Recognizing that the current algorithm cannot characterize every spectral shapes in nature, we stress the necessity to further enrich the data pool included in the LUT.

Acknowledgments

We thank the NASA Ocean Biology Processing Group and SeaBASS for processing the satellite remote sensing reflectance data and archiving and distributing the *in situ* matchup data. The principal investigators, including those responsible for AERONET-OC observatories, are appreciated for sharing their field measurements. Thanks are also due to the NOAA Center for

Satellite Applications and Research (STAR) and CoastWatch for processing and distributing the VIIRS-SNPP ocean color data. This study was co-funded by the NOAA VIIRS Ocean Color CAL/VAL project and the projects from the NASA Ocean Biology and Biogeochemistry (OBB) program and NASA Biological Diversity and Ecological Forecasting program. Four anonymous reviewers are thanked for comments and suggestions. The views, opinions, and findings contained in this paper are those of the authors and should not be construed as an official NOAA or U.S. Government position, policy, or decision.

The evaluation data used in this study are available upon request. Matlab scripts are provided to facilitate further assessment (https://github.com/Ocean-Color-Remote-Sensing-Algorithm/BBE/blob/master/blue_band_estimation.m and https://github.com/Ocean-Color-Remote-Sensing-Algorithm/BBE/blob/master/QAscores_5Bands.m).

References

Ahmad, Z., Franz, B.A., McClain, C.R., Kwiatkowska, E.J., Werdell, P.J., Shettle, E.P., & Holben, B.N. (2010). New aerosol models for the retrieval of aerosol optical thickness and normalized water-leaving radiances from the SeaWiFS and MODIS sensors over coastal regions and open oceans. *Applied Optics, 49*, 5545-5560.

Antoine, D., d'Ortenzio, F., Hooker, S.B., Be´cu, G., Gentili, B., Tailliez, D., & Scott, A.J. (2008). Assessment of uncertainty in the ocean reflectance determined by three satellite ocean color sensors (MERIS, SeaWiFS and MODIS-A) at an offshore site in the Mediterranean Sea (BOUSSOLE project). *Journal of Geophysical Research, 113*, C07013.

Antoine, D., & Morel, A. (1999). A multiple scattering algorithm for atmospheric correction of remotely sensed ocean colour (MERIS instrument): principle and implementation for atmospheres carrying various aerosols including absorbing ones. *International Journal of Remote Sensing, 20*, 1875-1916.

Bailey, S.W., Franz, B.A., & Werdell, P.J. (2010). Estimation of near-infrared water-leaving reflectance for satellite ocean color data processing. *Optics Express, 18*, 7521-7527.

Bailey, S.W., & Werdell, P.J. (2006). A multi-sensor approach for the on-orbit validation of ocean color satellite data products. *Remote Sensing of Environment, 102*, 12-23.

Banzon, V.F., Gordon, H.R., Kuchinke, C.P., Antoine, D., Voss, K.J., & Evans, R.H. (2009). Validation of a SeaWiFS dust-correction methodology in the Mediterranean Sea: Identification of an algorithm-switching criterion. *Remote Sensing of Environment, 113*, 2689-2700.

Behrenfeld, M.J., Boss, E., Siegel, D., & Shea, D.M. (2005). Carbon-based ocean productivity and phytoplankton physiology from space. *Global Biogeochemical Cycles, 19*, GB1006.

Bricaud, A., Babin, M., Morel, A., & Claustre, H. (1995). Variability in the chlorophyll-specific absorption coefficients of natural phytoplankton: Analysis and parameterization. *Journal of Geophysical Research, 100*, 13321-13332.

Bricaud, A., Claustre, H., Ras, J., & Oubelkheir, K. (2004). Natural variability of phytoplanktonic absorption in oceanic waters: Influence of the size structure of algal populations. *Journal of Geophysical Research, 109*, doi:10.1029/2004JC002419.

Bricaud, A., Morel, A., Babin, M., Allali, K., & Claustre, H. (1998). Variations of light absorption by suspended particles with chlorophyll a concentration in oceanic (case 1) waters: Analysis and implications for bio-optical models. *Journal of Geophysical Research, 103*, 31033-31044.

Carder, K.L., Chen, F.R., Lee, Z.P., Hawes, S.K., & Kamykowski, D. (1999). Semianalytic Moderate-resolution Imaging Spectrometer algorithms for chlorophyll-a and absorption with bio-optical domains based on nitrate-depletion temperatures. *Journal of Geophysical Research, 104*, 5403-5421.

Chomko, R.M., & Gordon, H.R. (2001). Atmospheric correction of ocean color imagery: test of the spectral optimization algorithm with the Sea-viewing Wide Field-of-View Sensor. *Applied Optics, 40*, 2973-2984.

D'Alimonte, D., Zibordi, G., & Mélin, F. (2008). A statistical method for generating cross-mission consistent normalized water-leaving radiances. *IEEE Transactions on Geoscience and Remote Sensing, 46*, 4075-4093.

Feng, H., Vandemark, D., Campbell, J.W., & Holben, B.N. (2008). Evaluation of MODIS ocean colour products at a northeast United States coast site near the Martha's Vineyard Coastal Observatory. *International Journal of Remote Sensing, 29*, 4479-4497.

Franz, B.A., Bailey, S.W., Eplee Jr, R.E., Lee, S., Patt, F.S., Proctor, C., & Meister, G. (2018). NASA multi-mission ocean color reprocessing 2018.0. In, *Ocean Optics XXIV*. Dubrovnik, Croatia

Gordon, H.R., Brown, O.B., Evans, R.H., Brown, J.W., Smith, R.C., Baker, K.S., & Clark, D.K. (1988). A semianalytic radiance model of ocean color. *Journal of Geophysical Research, 93*, 10909-10924.

Gordon, H.R., Du, T., & Zhang, T. (1997). Remote sensing of ocean color and aerosol properties: resolving the issue of aerosol absorption. *Applied Optics, 36*, 8670-8684.

Gordon, H.R., & Wang, M. (1994). Retrieval of water-leaving radiance and aerosol optical thickness over the oceans with SeaWiFS: a preliminary algorithm. *Applied Optics, 33*, 443-452.

He, X., Bai, Y., Pan, D., Tang, J., & Wang, D. (2012). Atmospheric correction of satellite ocean color imagery using the ultraviolet wavelength for highly turbid waters. *Optics Express, 20*, 20754-20770.

Hlaing, S., Harmel, T., Gilerson, A., Foster, R., Weidemann , A.D., Arnone, R., et al. (2013). Evaluation of the VIIRS ocean color monitoring performance in coastal regions. *Remote Sensing of Environment, 139*, 398-414.

Hooker, S.B., Lazin, G., Zibordi, G., & McLean, S. (2002). An evaluation of above- and in-water methods for determining water-leaving radiances. *Journal of Atmospheric and Oceanic Technology, 19*, 486-515.

Hu, C., Carder, K.L., & Mueller-Karger, F.E. (2000). Atmospheric correction of SeaWiFS imagery over turbid coastal waters: A practical method. *Remote Sensing of Environment, 74*, 195-206.

Hu, C., Feng, L., & Lee, Z.P. (2013). Uncertainties of SeaWiFS and MODIS remote sensing reflectance: implications from clear water measurements. *Remote Sensing of Environment, 133*, 168-182.

Hu, C., Lee, Z.P., & Franz, B. (2012). Chlorophyll a algorithms for oligotrophic oceans: a novel approach based on three-band reflectance difference. *Journal of Geophysical Research, 117*, 2156-2202.

Hyde, K.J.W., O'Reilly, J.E., & Oviatt, C.A. (2007). Validation of SeaWiFS chlorophyll a in Massachusetts Bay. *Continental Shelf Research, 27*, 1677-1691.

IOCCG (2006). Remote sensing of inherent optical properties: fundamentals, tests of algorithms, and applications. In Z.P. Lee (Ed.) (p. 126). Dartmouth, Nova Scotia, Canada: International Ocean Color Coordinating Group.

IOCCG (2010). Atmospheric correction for remotely-sensed ocean color products. In M. Wang (Ed.) (p. 78). Dartmouth, Nova Scotia, Canada: International Ocean Color Coordinating Group.

Jay, S., Guillaume, M., Chami, M., Minghelli, A., Deville, Y., Lafrance, B., & Serfaty, V. (2018). Predicting minimum uncertainties in the inversion of ocean color geophysical parameters based on Cramer-Rao bounds. *Optics Express, 26*, A1-A18.

Kahn, R.A., Sayer, A.M., Ahmad, Z., & Franz, B.A. (2016). The Sensitivity of SeaWiFS Ocean Color Retrievals to Aerosol Amount and Type. *Journal of Atmospheric and Oceanic Technology, 33*, 1185-1209.

Kruse, F.A., Lefkoff, A.B., Boardman, J.B., Heidebrecht, K.B., Shapiro, A.T., Barloon, P.J., & Goetz, A.F.H. (1993). The spectral image processing system (SIPS) - interactive visualization and analysis of imaging spectrometer data. *Remote Sensing of Environment, 44*, 145-163.

Lee, Z., Marra, J., Perry, M.J., & Kahru, M. (2015a). Estimating oceanic primary productivity from ocean color remote sensing: A strategic assessment. *Journal of Marine Systems, 149*, 50-59.

Lee, Z.P., Carder, K.L., & Arnone, R. (2002). Deriving inherent optical properties from water color: a multi-band quasi-analytical algorithm for optically deep waters. *Applied Optics, 41*, 5755-5772.

Lee, Z.P., Carder, K.L., Mobley, C.D., Steward, R.G., & Patch, J.S. (1998). Hyperspectral remote sensing for shallow waters. 1. A semianalytical model. *Applied Optics, 37*, 6329-6338.

Lee, Z.P., Wei, J., Voss, K.J., Lewis, M., Bricaud, A., & Huot, Y. (2015b). Hyperspectral absorption coefficient of "pure" seawater in the range of 350-550 nm inverted from remote sensing reflectance. *Applied Optics, 54*, 546-558.

Mannino, A., Novak, M.G., Hooker, S.B., Hyde, K., & Aurin, D. (2014). Algorithm development and validation of CDOM properties for esturine and continental shelf waters along the northeastern U.S. coast. *Remote Sensing of Environment, 152*, 576-602.

Mason, J.D., Cone, M.T., & Fry, E.S. (2016). Ultraviolet (250–550 nm) absorption spectrum of pure water. *Applied Optics, 55*, 7163-7172.

McClain, C.R. (2009). A decade of satellite ocean color observations. *Annual Review of Marine Science, 1*, 19-42.

Mélin, F., Zibordi, G., Berthon, J.-F., Bailey, S., Franz, B., Voss, K.J., et al. (2011). Assessment of MERIS reflectance data as processed with SeaDAS over the European seas. *Optics Express, 19*, 25657-25671.

Mikelsons, K., Wang, M., & Jiang, L. (2020). Statistical evaluation of satellite ocean color data retrievals. *Remote Sensing of Environment, 237*, 111601.
Morel, A., & Gentili, B. (2009). A simple band ratio technique to quantify the colored dissolved and detrital organic material from ocean color remotely sensed data. *Remote Sensing of Environment, 113* 998-1011.
Mouw, C.B., Greb, S., Aurin, D., DiGiacomo, P.M., Lee, Z., Twardowski, M., et al. (2015). Aquatic color radiometry remote sensing of coastal and inland waters: Challenges and recommendations for future satellite missions. *Remote Sensing of Environment, 160*, 15-30.
O'Reilly, J.E., Maritorena, S., Mitchell, B.G., Siegel, D., Carder, K.L., Garver, S., et al. (1998). Ocean color chlorophyll algorithms for SeaWiFS. *Journal of Geophysical Research, 103*, 24937-24953.
Oo, M., Vargas, M., Gilerson, A., Gross, B., Moshary, F., & Ahmed, S. (2008). Improving atmospheric correction for highly productive coastal waters using the short wave infrared retrieval algorithm with water-leaving reflectance constraints at 412nm. *Applied Optics, 47*, 3846-3859.
Qin, P., Simis, S.G.H., & Tilstone, G.H. (2017). Radiometric validation of atmospheric correction for MERIS in the Baltic Sea based on continuous observations from ships and AERONET-OC. *Remote Sensing of Environment, 200*, 263-280.
Ransibrahmanakul, V., & Stumpf, R.P. (2006). Correcting ocean colour refletance for absorbing aerosols. *International Journal of Remote Sensing, 27*, 1759-1774.
Sathyendranath, S., Lazzara, L., & Prieur, L. (1987). Variations in the spectral values of specific absorption of phytoplankton. *Limnology and Oceanography, 32*, 403-415.
Shettle, E.P., & Fenn, R.W. (1979). Models for the aerosols of the lower atmosphere and the effects of humidity variations on their optical properties. In, *Environmental Research Papers, No. 676* (p. 94). Manscom AFB, Massachusetts: U.S. Air Force Geophysics Laboratory, Air Force Systems Command, USAF.
Siegel, D.A., Wang, M., Maritorena, S., & Robinson, W. (2000). Atmospheric correction of satellite ocean color imagery: the black pixel assumption. *Applied Optics, 39*, 3582-3591.
Valente, A., Sathyendranath, S., Brotas, V., Groom, S., Grant, M., Taberner, M., et al. (2016). A compilation of global bio-optical in situ data for ocean-colour satellite applications. *Earth System Science Data, 8*, 235-252.
Wang, G., Lee, Z., & Mouw, C. (2017). Multi-Spectral Remote Sensing of Phytoplankton Pigment Absorption Properties in Cyanobacteria Bloom Waters: A Regional Example in the Western Basin of Lake Erie. *Remote Sensing, 9*, 1309.
Wang, M. (2007). Remote sensing of the ocean contributions from ultraviolet to near-infrared using the shortwave infrared bands: simulations. *Applied Optics, 46*, 1535-1547.
Wang, M., & Jiang, L. (2018). Atmospheric correction using the information from the short blue band. *IEEE Transactions on Geoscience and Remote Sensing, 56*, 6224-6237.
Wang, M., & Shi, W. (2005). Estimation of ocean contribution at the MODIS near-infrared wavelengths along the east coast of the U.S.: Two case studies. *Geophysical Research Letters, 32*, L13606.
Wang, M., & Shi, W. (2007). The NIR-SWIR combined atmospheric correction approach for MODIS ocean color data processing. *Optics Express, 15*, 15722-15733.
Wang, M., & Son, S. (2016). VIIRS-derived chlorophyll-a using the ocean color index method. *Remote Sensing of Environment, 182*, 141-149.

Wang, M., Son, S., & Shi, W. (2009). Evaluation of MODIS SWIR and NIR-SWIR atmospheric correction algorithm using SeaBASS data. *Remote Sensing of Environment, 113*, 635-644.

Wang, P., Boss, E., & Roesler, C.S. (2005). Uncertainties of inherent optical properties obtained from semianalytical inversions of ocean color. *Applied Optics, 44*, 4074-4085.

Wei, J., & Lee, Z.P. (2015). Retrieval of phytoplankton and color detrital matter absorption coefficients with remote sensing reflectance in an ultraviolet band. *Applied Optics, 54*, 636-649.

Wei, J., Lee, Z.P., Garcia, R.A., Zoffoli, M.L., Armstrong, R., Shang, Z., et al. (2018). An assessment of Landsat-8 atmospheric correction schemes and remote sensing reflectance products in coral reefs and coastal turbid waters. *Remote Sensing of Environment, 215*, 18-32.

Wei, J., Lee, Z.P., Ondrusek, M., Mannino, A., Tzortziou, M., & Armstrong, R. (2016a). Spectral slopes of the absorption coefficient of colored dissolved and detrital material inverted from UV-visible remote sensing reflectance. *Journal of Geophysical Research, 121*, 1953-1969.

Wei, J., Lee, Z.P., & Shang, S. (2016b). A system to measure the data quality of spectral remote sensing reflectance of aquatic environments. *Journal of Geophysical Research, 121*, 8189–8207.

Wei, J., Lee, Z.P., Shang, S., & Yu, X. (2019). Semianalytical derivation of phytoplankton, CDOM, and detritus absorption coefficients from the Landsat 8/OLI reflectance in coastal waters. *Journal of Geophysical Research, 124*, 3682-3699.

Werdell, P.J., & Bailey, S.W. (2005). An improved bio-optical data set for ocean color algorithm development and satellite data product validation. *Remote Sensing of Environment, 98*, 122-140.

Werdell, P.J., Franz, B.A., Bailey, S.W., Feldman, G.C., Boss, E., Brando, V.E., et al. (2013). Generalized ocean color inversion model for retrieving marine inherent optical properties. *Applied Optics, 52*, 2019-2037.

Werdell, P.J., McKinna, L.I.W., Boss, E., Ackleson, S.G., Craig, S.E., Gregg, W.W., et al. (2018). An overview of approaches and challenges for retrieving marine inherent optical properties from ocean color remote sensing. *Progress in Oceanography, 160*, 186-212.

Yu, X., Shen, F., & Liu, Y. (2016). Light absorption properties of CDOM in the Changjiang (Yangtze) estuarine and coastal waters: An alternative approach for DOC estimation. *Estuarine, Coastal and Shelf Science, 181*, 302-311.

Zhang, X.D., & Hu, L.B. (2009). Estimating scattering of pure water from density fluctuation of the refractive index. *Optics Express, 17*, 1671-1678.

Zibordi, G., Berthon, J.-F., Mélin, F., D'Alimonte, D., & Kaitala, S. (2009). Validation of satellite ocean color primary products at optically complex coastal sites: Northern Adriatic Sea, Northern Baltic Proper and Gulf of Finland. *Remote Sensing of Environment, 113* 2574-2591.

List of Figure Captions

Figure 1. Satellite matchup stations for SeaWiFS (denoted by open circles "○"), MODISA (denoted by crosses "+"), and VIIRS-SNPP (denoted by open diamonds "◊") in the global oceans. The background image refers to the annual chlorophyll-a concentration for 2010 derived from SeaWiFS.

Figure 2. Frequency distribution of the QA scores for SeaWiFS, MODISA, and VIIRS-SNPP $R_{rs}(\lambda)$ data. The QA scores are calculated based on the five "common" bands of 41x, 443, 48x, 55x, and 67x nm.

Figure 3. Ranges of $nR_{rs}(\lambda)$ values used in different data sets. Note that the in situ matchup data are used to describe the variability of corresponding satellite missions in order to avoid the negative nR_{rs}(41x) values.

Figure 4. Normalized remote sensing reflectance spectra representative of three distinctive optical water classes based on the IOCCG (2006) $R_{rs}(\lambda)$ data at 412, 443, 488, 551, and 670 nm. The shaded areas describe the range of variation of the spectral values of $nR_{rs}(\lambda)$.

Figure 5. Comparison of moderate-QA (0.4 The shaded areas desc$R_{rs}(\lambda)$ data and in situ measurements at 41x and 443 nm bands. The symbols of red "○" and blue "+" denote the results before and after the implementation of the BBE algorithm. Linear regression results are also plotted for two data sets. Note that the scatterplots have included all available data points, positive and negative.

Figure 6. Comparison of moderate-QA ($0.4 \leqslant$ QA $\leqslant 0.6$) satellite $R_{rs}(\lambda)$ spectral ratios with in situ matchups. The symbols of red lite l available data points, positive and negative. the implementation of the BBE algorithm. Linear regression results are also plotted for two data sets. Note that the scatterplots have included all available data points, positive and negative.

Figure 7. Uncertainty of estimated Rrs(412) and Rrs(443) induced by erroneous Rrs(λ) at 488, 551, or 670 nm bands. The first, second, and third rows refer to Class 1, Class 2, and Class 3 waters, respectively, corresponding to Figure 4.

Figure 8. Percentage of moderate-QA and low-QA satellite data in (a) the U.S. west coasts (b) the U.S. east coasts. The two highlighted areas are (c) the Vancouver Island and (d) Massachusetts Bay and the Gulf of Maine. The percentage data shown here are derived from the MODISA Level 3 mapped (9 km) daily remote sensing reflectance products in 2003, with the QA scores computed based on the $R_{rs}(\lambda)$ at five bands (412, 443, 488, 547, and 667 nm).

Figure 9. (a) VIIRS-SNPP R_{rs}(410) image in the northern Gulf of Mexico (Image id: V2016048190213_NPP_SCINIR_L2). (b) The same image but with estimated R_{rs}(410) for moderate- and low-QA pixels. White pixels indicate the failure of quality checks for land, cloud,

stray light, high glint, and/or high TOA, etc. The dashed line in (a) indicates where the strongly absorbing aerosols occur, and the negative $R_{rs}(410)$ values are likely to present, according to the quality flags.

Table 1. Synthesized combinations of absolute percentage errors |ε| for $R_{rs}(488)$, $R_{rs}(551)$, and $R_{rs}(670)$ data for uncertainty analysis.

	Class 1 (N = 173)			Class 2 (N = 137)			Class 3 (N = 190)		
	$R_{rs}(488)$	$R_{rs}(551)$	$R_{rs}(670)$	$R_{rs}(488)$	$R_{rs}(551)$	$R_{rs}(670)$	$R_{rs}(488)$	$R_{rs}(551)$	$R_{rs}(670)$
1	0	0	0	0	0	0	0	0	0
2	5%	5%	20%	15%	10%	20%	15%	10%	15%
3	10%	15%	30%	20%	15%	30%	20%	15%	20%
4	20%	20%	45%	25%	20%	35%	25%	20%	25%
5	30%	20%	60%	30%	20%	40%	30%	25%	30%

* The chlorophyll-a concentration (± standard deviation) for each water class is as below: Class 1, Chl = 0.14 (± 0.13) mg m^{-3}; Class 2, Chl = 1.6 (± 1.8) mg m^{-3}; Class 3, Chl = 15 (± 9) mg m^{-3}.

Table 2. Uncertainties of satellite $R_{rs}(\lambda)$ values at three wavelengths (48x, 55x, and 67x nm) generated from SeaWiFS, MODISA, and VIIRS-SNPP in the global waters. The uncertainties are calculated based upon the satellite and *in situ* matchups. The data are divided into three subgroups according to the QA scores of the satellite $R_{rs}(\lambda)$ spectra. Negative values are excluded from analysis.

		SeaWiFS			MODISA			VIIRS-SNPP		
		$R_{rs}(490)$	$R_{rs}(555)$	$R_{rs}(670)$	$R_{rs}(488)$	$R_{rs}(547)$	$R_{rs}(667)$	$R_{rs}(486)$	$R_{rs}(551)$	$R_{rs}(671)$
QA ≤ 0.2	$\lvert\bar{\varepsilon}\rvert$	46%	23%	21%	40%	22%	28%	34%	27%	48%
	$\bar{\varepsilon}$	-45%	-23%	-19%	-37%	-21%	-26%	-19%	-17%	-24%
	RMSD [1]	0.0011	0.0006	0.0002	0.0007	0.0006	0.0002	0.0009	0.0005	0.0002
	N [*]	92	95	81	101	101	91	24	24	22
0.4 ≤ QA ≤ 0.6	$\lvert\bar{\varepsilon}\rvert$	18%	15%	11%	24%	16%	37%	18%	11%	23%
	$\bar{\varepsilon}$	-10%	-7%	0%	-20%	-15%	-31%	-5%	-5%	-1%
	RMSD	0.0006	0.0004	0.0000	0.0007	0.0005	0.0002	0.0004	0.0003	0.0002
	N	359	359	321	576	576	515	239	239	236
QA ≥ 0.8	$\lvert\bar{\varepsilon}\rvert$	10%	11%	11%	13%	11%	22%	13%	11%	20%
	$\bar{\varepsilon}$	0%	-4%	0%	-10%	-9%	-16%	-10%	-9%	2%
	RMSD	0.0004	0.0004	0.0001	0.0005	0.0005	0.0002	0.0006	0.0005	0.0002
	N	2055	2055	1999	2932	2932	2866	2148	2148	2134

[1] RMSD is given in absolute units of sr^{-1}.

Table 3. Uncertainties of satellite $R_{rs}(\lambda)$ values at two blue bands (41x and 443 nm) generated from SeaWiFS, MODISA, and VIIRS-SNPP in the global waters. The uncertainties are calculated based upon the satellite and *in situ* matchups. The data are divided into three subgroups according to the QA scores of the satellite $R_{rs}(\lambda)$ spectra. Negative values are excluded from analysis.

Original data							
		SeaWiFS		MODISA		VIIRS-SNPP	
		$R_{rs}(412)$	$R_{rs}(443)$	$R_{rs}(412)$	$R_{rs}(443)$	$R_{rs}(410)$	$R_{rs}(443)$
QA ≤ 0.2	$\lvert\bar{\varepsilon}\rvert$	82%	71%	89%	62%	80%	32%
	$\bar{\varepsilon}$	-52%	-64%	10%	-52%	42%	11%
	RMSD	0.0024	0.0017	0.0018	0.0007	0.0016	0.0008
	N	29	61	35	75	23	23
0.4 ≤ QA ≤ 0.6	$\lvert\bar{\varepsilon}\rvert$	22%	31%	51%	38%	83%	38%
	$\bar{\varepsilon}$	0%	-14%	-8%	-11%	36%	20%
	RMSD	0.0009	0.0008	0.0010	0.0007	0.0013	0.0007
	N	279	346	450	561	235	239
QA ≥ 0.8	$\lvert\bar{\varepsilon}\rvert$	17%	18%	27%	17%	28%	19%
	$\bar{\varepsilon}$	0%	4%	3%	3%	7%	5%
	RMSD	0.0007	0.0007	0.0006	0.0005	0.0008	0.0006
	N	2049	2055	2913	2932	2148	2148
BBE-estimated data							
		SeaWiFS		MODISA		VIIRS-SNPP	
		$R_{rs}(412)$	$R_{rs}(443)$	$R_{rs}(412)$	$R_{rs}(443)$	$R_{rs}(410)$	$R_{rs}(443)$
QA ≤ 0.2	$\lvert\bar{\varepsilon}\rvert$	59%	39%	51%	36%	52%	42%
	$\bar{\varepsilon}$	30%	-17%	-3%	-17%	21%	4%
	RMSD	0.0008	0.0006	0.0004	0.0004	0.0012	0.0009
	N	95	95	101	101	24	24
0.4 ≤ QA ≤ 0.6	$\lvert\bar{\varepsilon}\rvert$	36%	23%	39%	30%	41%	28%
	$\bar{\varepsilon}$	8%	-4%	-6%	-13%	18%	10%
	RMSD	0.0009	0.0007	0.0006	0.0005	0.0006	0.0005
	N	359	359	576	576	239	239
QA ≥ 0.8	$\lvert\bar{\varepsilon}\rvert$	22%	17%	28%	18%	27%	19%
	$\bar{\varepsilon}$	-1%	-2%	0%	-2%	1%	0%
	RMSD	0.0009	0.0007	0.0006	0.0005	0.0007	0.0005
	N	2055	2055	2932	2932	2148	2148

Table 4. Uncertainties of satellite retrieved $R_{rs}(\lambda)$ spectral ratios, R_{443}^{41x} and R_{55x}^{443}, for SeaWiFS, MODISA, and VIIRS-SNPP in the global waters. The uncertainties are calculated based upon the satellite and *in situ* matchups. The data are divided into three subgroups according to the QA scores of the satellite $R_{rs}(\lambda)$ spectra. Negative values are excluded from analysis.

With orignal R_{rs}(41x) and R_{rs}(443) data							
		SeaWiFS		MODISA		VIIRS-SNPP	
		R_{555}^{443}	R_{443}^{412}	R_{547}^{443}	R_{443}^{412}	R_{551}^{443}	R_{443}^{410}
QA ≤ 0.2	$\lvert\varepsilon\rvert$	62%	60%	53%	58%	44%	39%
	$\bar{\varepsilon}$	-52%	-32%	-38%	34%	44%	33%
	RMSD	0.4495	0.4718	0.2224	0.5126	0.4925	0.4135
	N	61	29	75	35	23	23
0.4 ≤ QA ≤ 0.6	$\lvert\varepsilon\rvert$	24%	16%	36%	25%	37%	43%
	$\bar{\varepsilon}$	-4%	-3%	3%	-7%	30%	10%
	RMSD	0.2452	0.1455	0.1982	0.2159	0.2358	0.3329
	N	346	279	561	450	239	235
QA ≥ 0.8	$\lvert\varepsilon\rvert$	17%	9%	17%	12%	18%	12%
	$\bar{\varepsilon}$	11%	-1%	13%	-1%	15%	1%
	RMSD	0.1848	0.0812	0.1053	0.1015	0.1272	0.1002
	N	2055	2049	2932	2913	2148	2148
With BBE-estimated R_{rs}(41x) and R_{rs}(443) data							
		SeaWiFS		MODISA		VIIRS-SNPP	
		R_{555}^{443}	R_{443}^{412}	R_{547}^{443}	R_{443}^{412}	R_{551}^{443}	R_{443}^{410}
QA ≤ 0.2	$\lvert\varepsilon\rvert$	35%	41%	29%	29%	31%	23%
	$\bar{\varepsilon}$	6%	36%	-3%	25%	16%	3%
	RMSD	0.1615	0.3145	0.0940	0.2298	0.3699	0.2163
	N	95	95	101	101	24	24
0.4 ≤ QA ≤ 0.6	$\lvert\varepsilon\rvert$	18%	20%	22%	16%	25%	18%
	$\bar{\varepsilon}$	0%	11%	1%	5%	18%	5%
	RMSD	0.1988	0.1838	0.1288	0.1390	0.1405	0.1672
	N	359	359	576	576	239	239
QA ≥ 0.8	$\lvert\varepsilon\rvert$	15%	12%	16%	13%	16%	13%
	$\bar{\varepsilon}$	4%	0%	7%	1%	9%	1%
	RMSD	0.1594	0.1125	0.0938	0.1123	0.1057	0.1149
	N	2055	2055	2932	2932	2148	2148

Table 5. Combined uncertainty for the estimated $R_{rs}(412)$ and $R_{rs}(443)$ as a result of the uncertainty propagation from the input $R_{rs}(\lambda)$ spectra at 488, 551, and 670 nm. The uncertainties for the input $R_{rs}(\lambda)$ spectra are tabulated in Table 1.

			$R_{rs}(412)$				$R_{rs}(443)$			
	Chl	No.	$\lvert\bar{\varepsilon}\rvert$	$\bar{\varepsilon}$	RMSD	N	$\lvert\bar{\varepsilon}\rvert$	$\bar{\varepsilon}$	RMSD	N
Class 1	0.14±0.13 mg m^{-3}	1	13%	-10%	0.0020	173	7%	-5%	0.0009	173
		2	16%	-6%	0.0021		10%	-4%	0.0011	
		3	25%	-4%	0.0035		17%	-2%	0.0021	
		4	40%	-1%	0.0057		32%	0%	0.0036	
		5	56%	-1%	0.0077		47%	1%	0.0051	
Class 2	1.6±1.8 mg m^{-3}	1	9%	-2%	0.0008	137	4%	-1%	0.0004	137
		2	28%	-3%	0.0015		22%	0%	0.0012	
		3	35%	-3%	0.0019		29%	-1%	0.0016	
		4	41%	-2%	0.0023		35%	-1%	0.0020	
		5	46%	-2%	0.0027		40%	-1%	0.0023	
Class 3	15±9 mg m^{-3}	1	13%	1%	0.0008	190	6%	0%	0.0005	190
		2	30%	11%	0.0011		22%	8%	0.0009	
		3	37%	18%	0.0013		27%	12%	0.0011	
		4	43%	24%	0.0016		31%	16%	0.0014	
		5	47%	30%	0.0018		35%	20%	0.0016	

Table 6. Uncertainties of $a_{ph}(443)$ and $a_{dg}(443)$ derived from the original satellite $R_{rs}(\lambda)$ data and estimated $R_{rs}(\lambda)$ data at blue bands. The uncertainties are calculated with regard to the retrievals from corresponding *in situ* $R_{rs}(\lambda)$. All negative R_{rs}(41x) and $R_{rs}(443)$ values and negative $a_{ph}(443)$ and $a_{dg}(443)$ retrievals are excluded from the comparison. Negative values are excluded from analysis.

With orignal R_{rs}(41x) and $R_{rs}(443)$ data							
		SeaWiFS		MODISA		VIIRS-SNPP	
		$a_{ph}(443)$	$a_{dg}(443)$	$a_{ph}(443)$	$a_{dg}(443)$	$a_{ph}(443)$	$a_{dg}(443)$
QA ≤ 0.2	$\lvert\bar{\Phi}\rvert$	46%	136%	56%	142%	38%	132%
	$\bar{\Phi}$	0%	34%	-12%	4%	-4%	-91%
	RMSD	0.0213	0.2878	0.0464	0.3031	0.0195	0.0359
	N	7	29	16	28	15	19
0.4 ≤ QA ≤ 0.6	$\lvert\bar{\Phi}\rvert$	48%	64%	67%	89%	47%	117%
	$\bar{\Phi}$	-26%	15%	-42%	-3%	-10%	-24%
	RMSD	0.0070	0.0179	0.0324	0.0679	0.0334	0.2291
	N	169	268	261	418	116	190
QA ≥ 0.8	$\lvert\bar{\Phi}\rvert$	44%	42%	49%	58%	41%	57%
	$\bar{\Phi}$	-21%	-4%	-21%	-13%	-10%	-11%
	RMSD	0.0155	0.0144	0.0314	0.0494	0.0260	0.0477
	N	1786	2024	2258	2873	1685	2088
With BBE-estimated R_{rs}(41x) and $R_{rs}(443)$ data							
		SeaWiFS		MODISA		VIIRS-SNPP	
		$a_{ph}(443)$	$a_{dg}(443)$	$a_{ph}(443)$	$a_{dg}(443)$	$a_{ph}(443)$	$a_{dg}(443)$
QA ≤ 0.2	$\lvert\bar{\Phi}\rvert$	87%	105%	78%	82%	58%	72%
	$\bar{\Phi}$	34%	-15%	33%	-14%	-55%	12%
	RMSD	0.1908	0.3423	0.1680	0.2426	0.0249	0.0524
	N	55	107	66	118	15	20
0.4 ≤ QA ≤ 0.6	$\lvert\bar{\Phi}\rvert$	51%	66%	59%	59%	62%	69%
	$\bar{\Phi}$	5%	-16%	-19%	5%	-32%	-21%
	RMSD	0.0102	0.0333	0.0367	0.0694	0.0435	0.0868
	N	202	345	327	548	118	219
QA ≥ 0.8	$\lvert\bar{\Phi}\rvert$	45%	48%	50%	57%	49%	56%
	$\bar{\Phi}$	-13%	0%	-13%	-11%	-8%	-7%
	RMSD	0.0155	0.0211	0.0320	0.0566	0.0306	0.0532
	N	1791	2030	2268	2907	1685	2102

List of Figure Captions

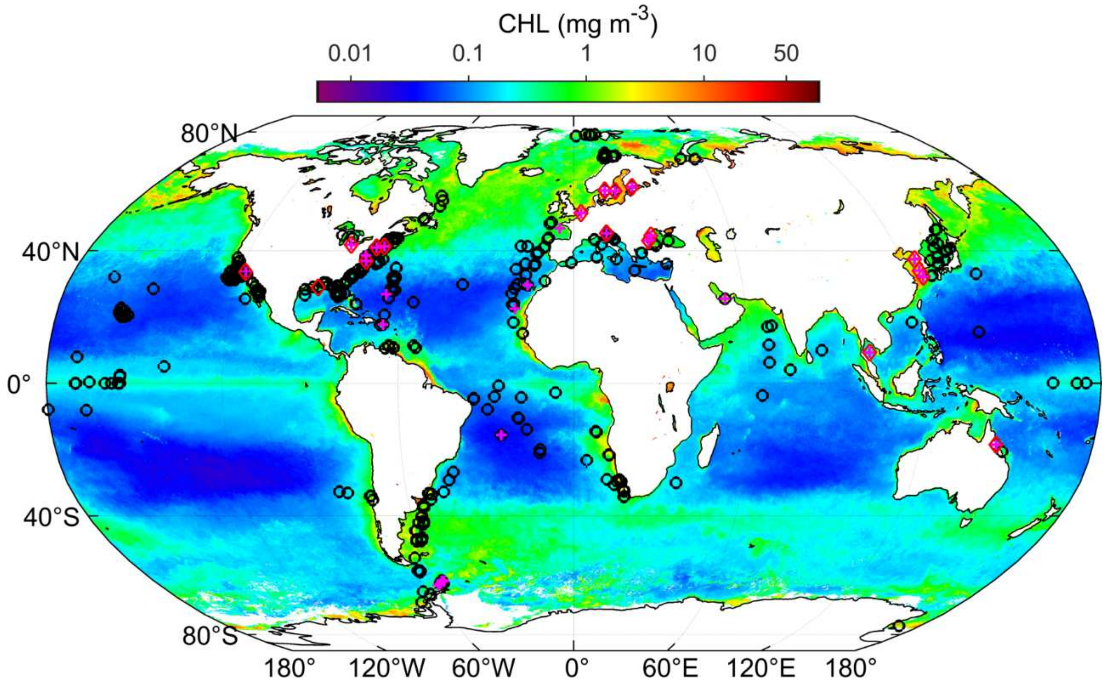

Figure 1. Satellite matchup stations for SeaWiFS (denoted by open circles "○"), MODISA (denoted by crosses "+"), and VIIRS-SNPP (denoted by open diamonds "◊") in the global oceans. The background image refers to the annual chlorophyll-a concentration for 2010 derived from SeaWiFS.

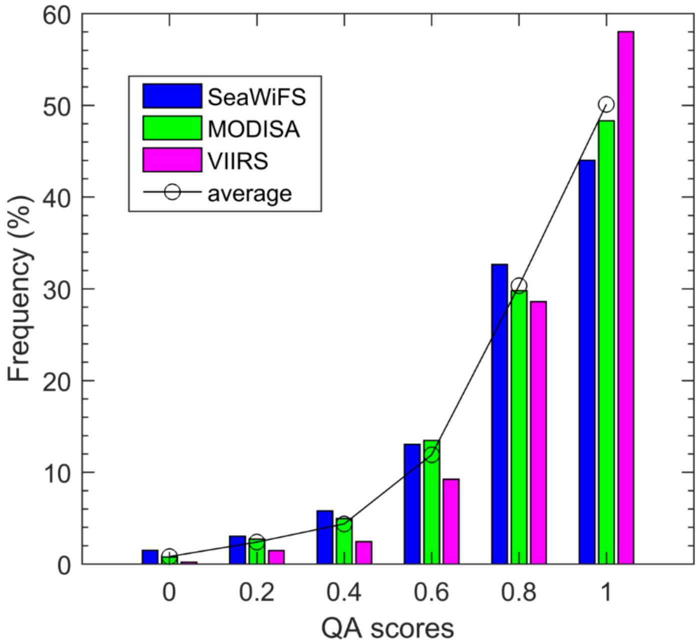

Figure 2. Frequency distribution of the QA scores for SeaWiFS, MODISA, and VIIRS-SNPP $R_{rs}(\lambda)$ data. The QA scores are calculated based on the five "common" bands of 41x, 443, 48x, 55x, and 67x nm.

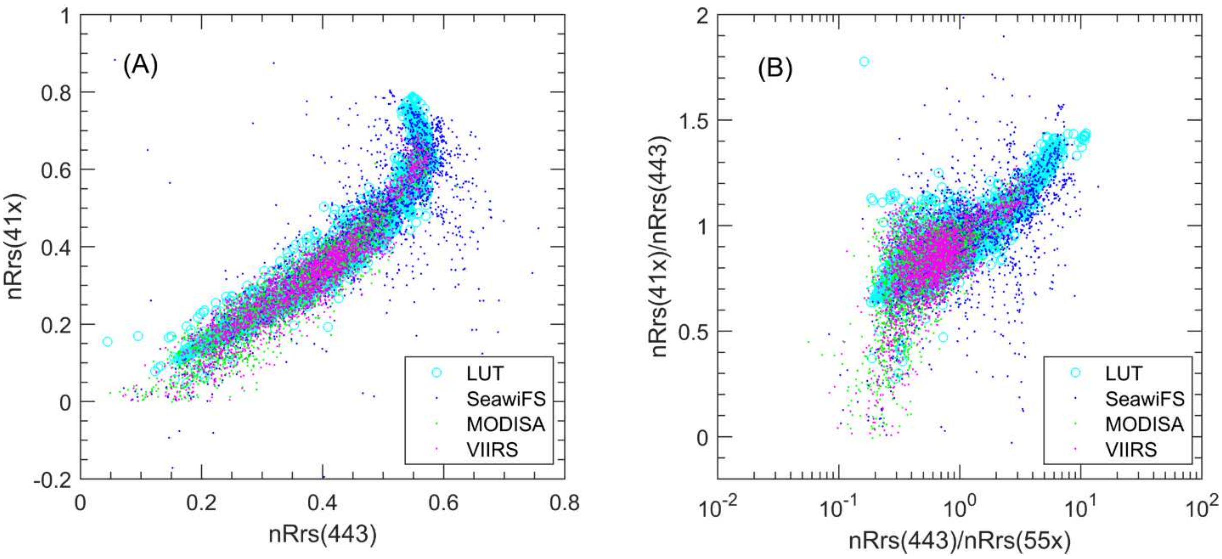

Figure 3. Ranges of $nR_{rs}(\lambda)$ values used in different data sets. Note that the *in situ* matchup data are used to describe the variability of corresponding satellite missions in order to avoid the negative nR_{rs}(41x) values.

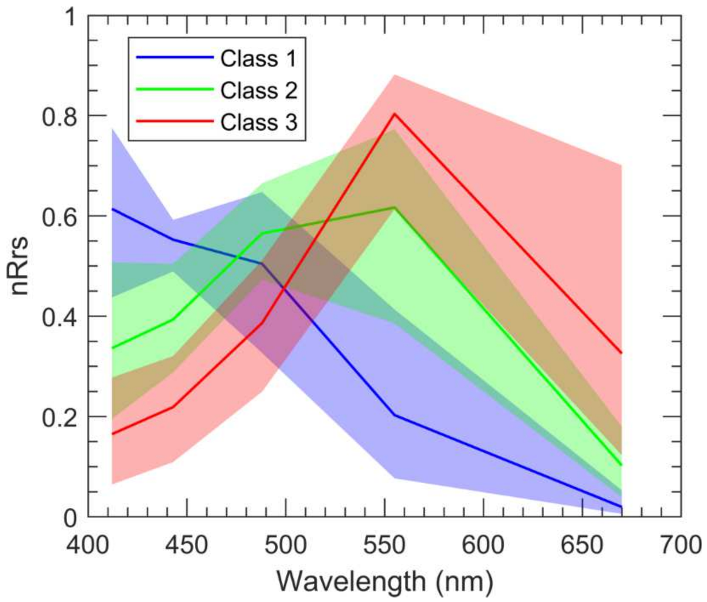

Figure 4. Normalized remote sensing reflectance spectra representative of three distinctive optical water classes based on the IOCCG (2006) $R_{rs}(\lambda)$ data at 412, 443, 488, 551, and 670 nm. The shaded areas describe the range of variation of the spectral values of $nR_{rs}(\lambda)$.

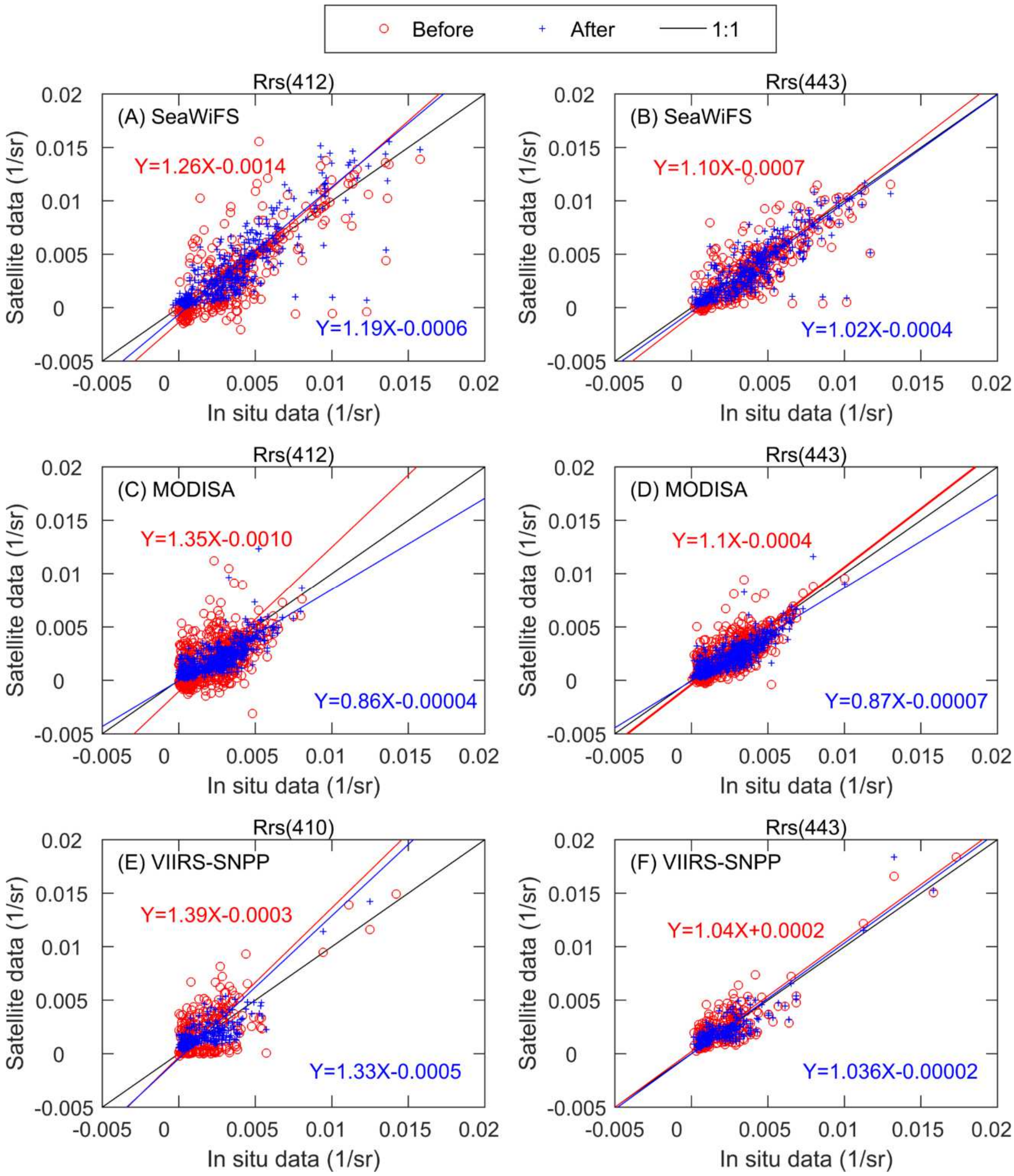

Figure 5. Comparison of moderate-QA (0.4 ≤ QA ≤ 0.6) satellite $R_{rs}(\lambda)$ data and *in situ* measurements at 41x and 443 nm bands. The symbols of red "○" and blue "+" denote the results before and after the implementation of the BBE algorithm. Linear regression results are also plotted for two data sets. Note that the scatterplots have included all available data points, positive and negative.

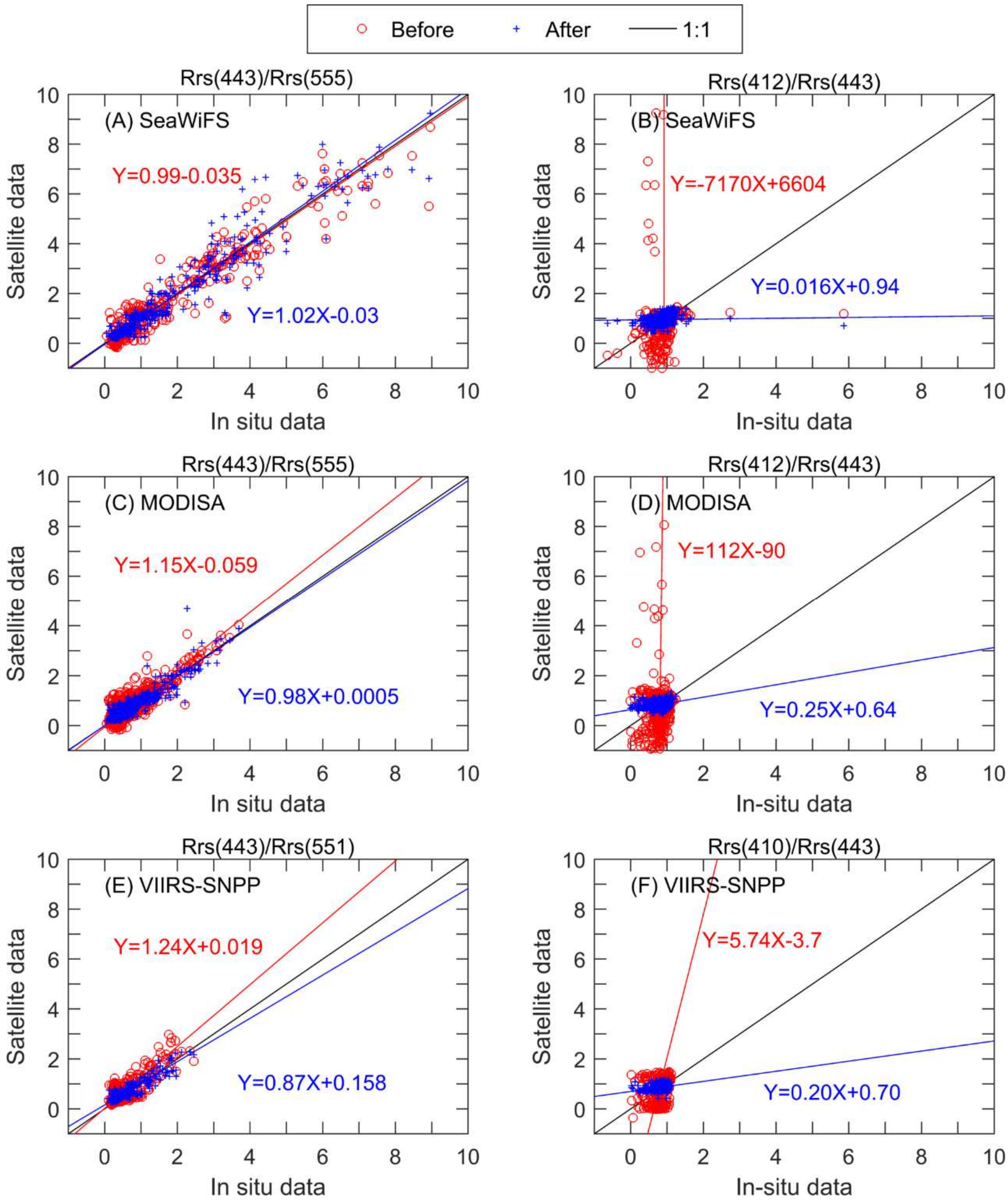

Figure 6. Comparison of moderate-QA ($0.4 \leq QA \leq 0.6$) satellite $R_{rs}(\lambda)$ spectral ratios with *in situ* matchups. The symbols of red "○" and blue "+" denote the results before and after the implementation of the BBE algorithm. Linear regression results are also plotted for two data sets. Note that the scatterplots have included all available data points, positive and negative.

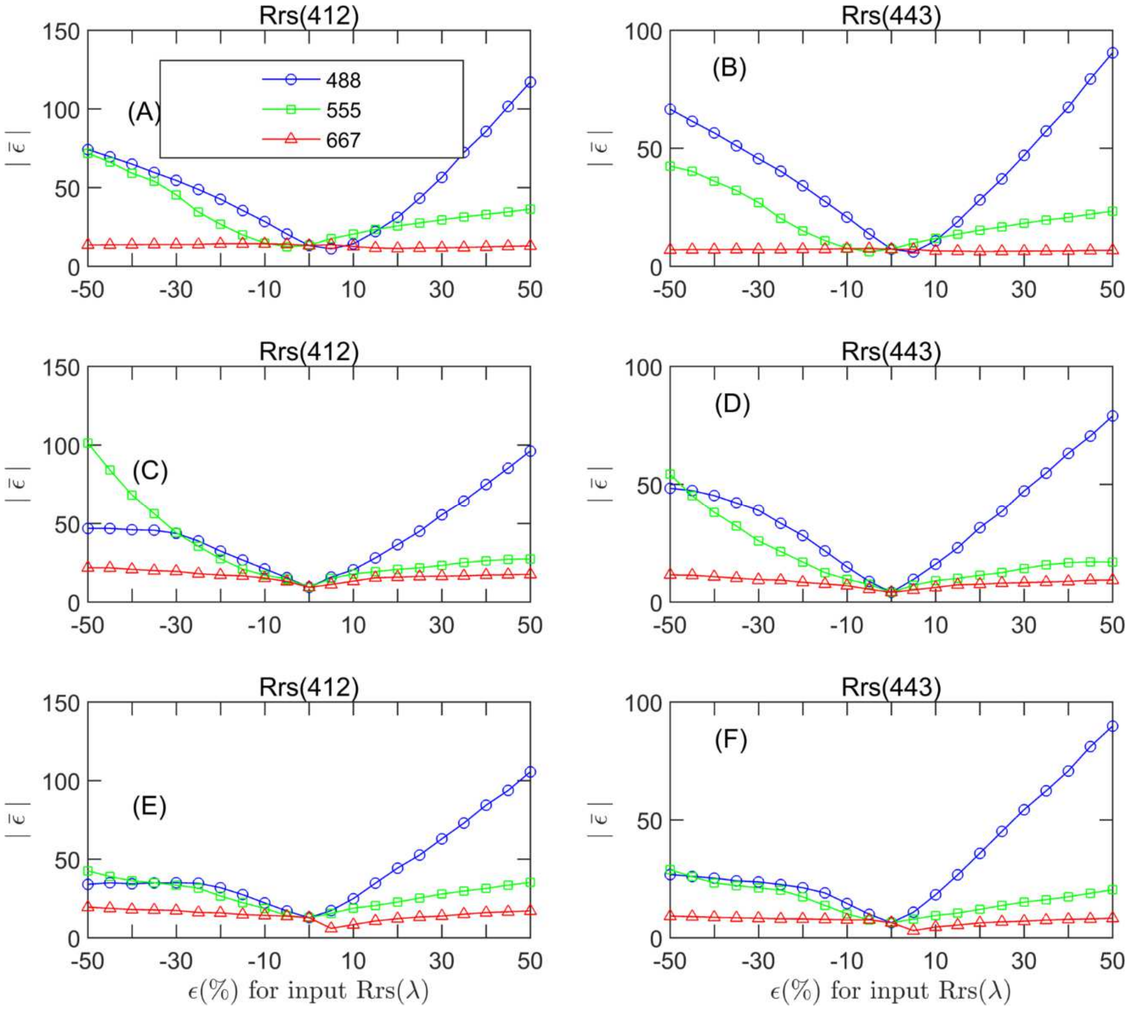

Figure 7. Uncertainty of estimated $R_{rs}(412)$ and $R_{rs}(443)$ induced by erroneous $R_{rs}(\lambda)$ at 488, 551, or 670 nm bands. The first, second, and third rows refer to Class 1, Class 2, and Class 3 waters, respectively, corresponding to Figure 4.

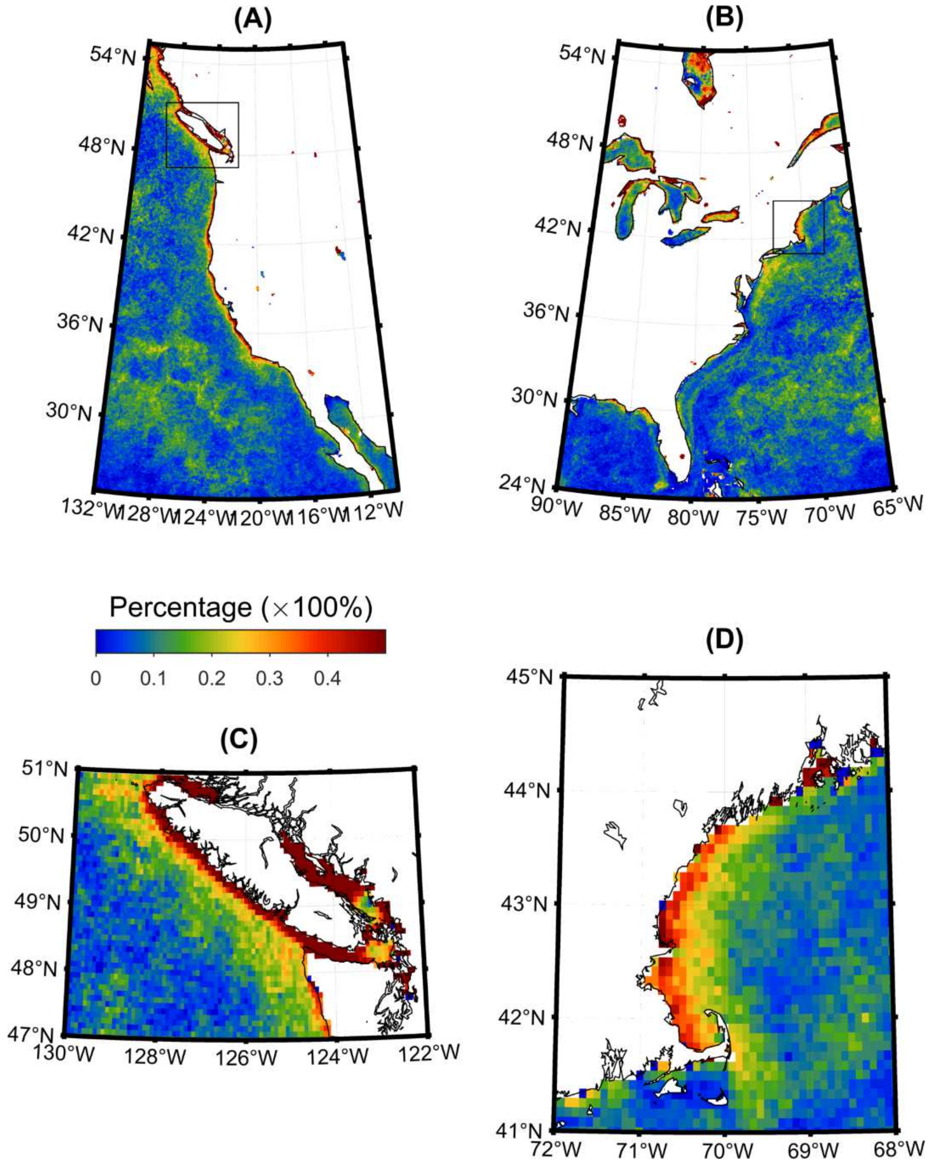

Figure 8. Percentage of moderate-QA and low-QA satellite data in (a) the U.S. west coasts and inland waters; and (b) the U.S. east coasts and inland waters. The two highlighted areas are (c) the Vancouver Island and (d) Massachusetts Bay and the Gulf of Maine. The percentage data shown here are derived from the MODISA Level 3 mapped (9 km) daily remote sensing reflectance products in 2003, with the QA scores computed based on the R_{rs} at five bands (412, 443, 488, 547, and 667 nm).

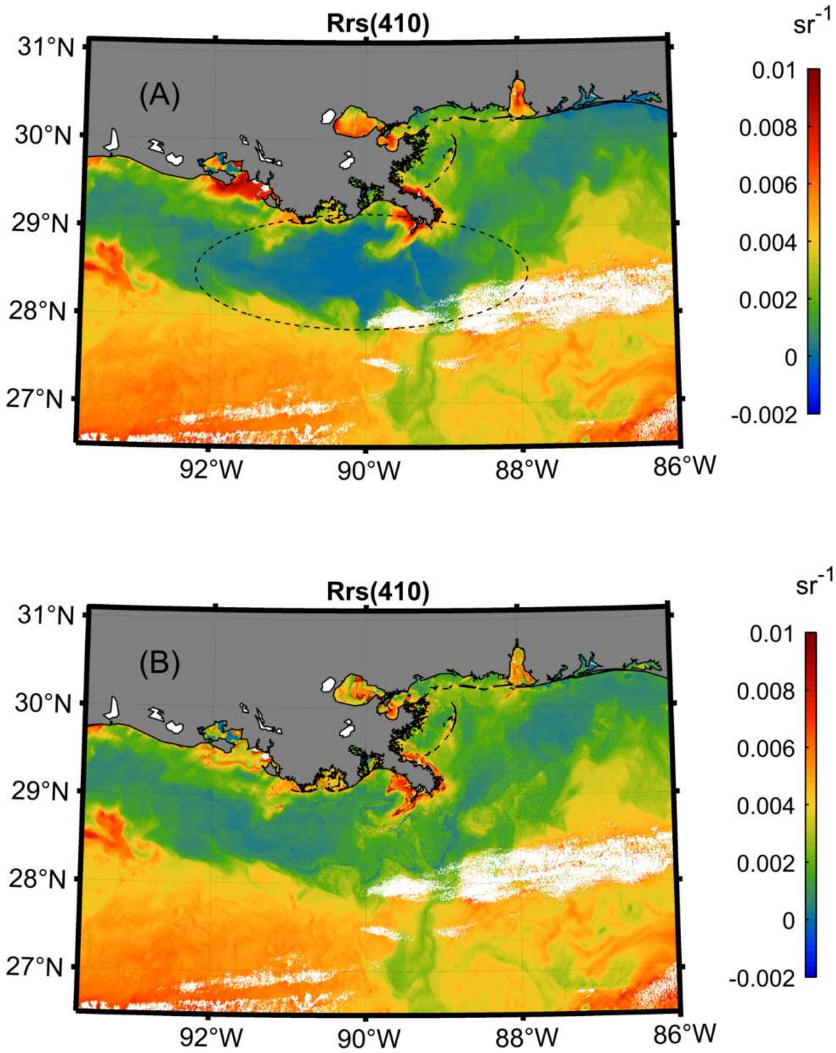

Figure 9. (a) VIIRS-SNPP R_{rs}(410) image in the northern Gulf of Mexico (Image id: V2016048190213_NPP_SCINIR_L2). (b) The same image but with estimated R_{rs}(410) for moderate- and low-QA pixels. White pixels indicate the failure of quality checks for land, cloud, stray light, high glint, and/or high TOA, etc. The dashed line in (a) indicates where the strongly absorbing aerosols occur, and the negative R_{rs}(410) values are likely to present, according to the quality flags.